Yang, L., Gómez García, R., Fan, M. & Zhang, R. 2022, "Multilayered input-reflectionless quasi-elliptic-type wideband bandpass filtering devices on diplexer-based structures", IEEE Transactions on Microwave Theory and Techniques, vol. 70, no. 1, pp. 122-138.

Available at http://dx.doi.org/10.1109/TMTT.2021.3121013

Multilayered Input-Reflectionless Quasi-Elliptic-Type Wideband Bandpass Filtering Devices on Diplexer-Based Structures

Li Yang, *Member, IEEE*, Roberto Gómez-García, *Senior Member, IEEE*, Maoyu Fan, and Runqi Zhang, *Member, IEEE*

***Abstract*— Classes of input-reflectionless wideband bandpass filters (BPFs) and balun BPF with quasi-elliptic-type (QET) responses are reported. They consist of two signal-transmission parts in multilayered diplexer-based topologies, as follows: 1) a BPF channel shaped by a two-/three-port reflective-type BPF/balun on a microstrip-to-microstrip vertical transition and 2) an input-absorptive bandstop filter (BSF) channel built with a shunt resistively terminated lowpass filter (LPF) that is composed of hybrid microstrip sections and open-circuit-ended microstrip stubs. Two real-frequency out-of-band transmission zeros (TZs) are generated in these RF filtering devices using a cascaded short-circuit-ended two-section microstrip line and two shunt open-circuit-ended half-wavelength microstrip lines, respectively. Using a higher order LPF network, enhanced passband amplitude flatness and improved stopband power absorption ratio levels for the devised BPFs are attained. As design examples, two third-order BPFs with a shunt resistively terminated microstrip T-junction and a π-shape structure, respectively, are first provided. Afterward, a higher order BPF based on two cascaded replicas of a third-order BPF unit is designed to show highly increased stopband power attenuation levels and enhanced power absorption ratio profile within the stopband-to-passband transitions. Subsequently, their application to an input-absorptive QET fourth-order wideband balun BPF is presented. The operational principles of these BPFs and balun are detailed by the developed design procedures, in which their associated impedance-type design parameters are synthetically determined. As practical validation, four microstrip prototypes corresponding to three 2-GHz wideband BPFs and one 1-GHz broadband balun BPF are manufactured and tested. These input-reflectionless wideband filtering components experimentally feature the desired merits in terms of QET responses, enhanced passband amplitude flatness, and improved stopband power absorption ratio levels.**

***Index Terms*— Absorptive filter, balun, bandpass filter (BPF), diplexer-based topology, multilayered circuit, power absorption ratio, quasi-elliptic-type (QET) response, transmission zero (TZ), vertical transition, wideband filter.**

Manuscript received May 27, 2021; revised September 18, 2021; accepted September 29, 2021. This work was supported in part by the Spanish Ministry of Economy, Industry, and Competitiveness (State Research Agency) under Project PID2020-116983RB-I00 and in part by the GOT ENERGY TALENT (GET) fellowship program co-funded by the EU as part of the H2020-MSCA-COFUND program under Grant 754382. This article is an expanded version from the 2020 Asia-Pacific Microwave Conference (APMC2020), Hong Kong, Dec. 8–11, 2020 [DOI: 10.1109/APMC47863.2020.9331419]. *(Corresponding authors: Li Yang; Roberto Gómez-García.)*

Li Yang and Roberto Gómez-García are with the Department of Signal Theory and Communications, University of Alcalá, Polytechnic School, Alcalá de Henares, 28871 Madrid, Spain (e-mail: yang96507@gmail.com; roberto.gomez.garcia@ieee.org).

Maoyu Fan is with the EHF Key Laboratory of Science, School of Electronic Science and Engineering, University of Electronic Science and Technology of China, Chengdu 611731, China (e-mail: ljkasuo@126.com).

Runqi Zhang is with the Akoustis, Inc., Huntersville, NC 28078 USA (e-mail: rzhang1@e.ntu.edu.sg).

Color versions of one or more figures in this article are available at https://doi.org/10.1109/TMTT.2021.3121013.

Digital Object Identifier 10.1109/TMTT.2021.3121013

I. Introduction

REFLECTIONLESS bandpass filters (BPFs) have lately attracted a tremendous attention, owing to their intrinsic merits of effectively mitigating the harmful effect of undesired RF signal power echoes in the active stages of complete RF front-end chains so as to improve their operational robustness [1]. Compared with more conventional reflective-type BPFs, the nontransmitted RF input signal energy at their stopband regions is expected to be mostly dissipated inside the lossy structures of absorptive/reflectionless BPFs instead of being reflected back to the source [2]. Hence, they could be a preferred alternative solution with regard to other typically adopted techniques to avoid the presence of unwanted RF signal power reflections (e.g., the use of interblock RF active/passive isolators or attenuation stages) toward more compact energy-efficient RF transceiver architectures [3].

Up to now, input- and two-port-reflectionless BPF devices exploiting different design methodologies have been reported, such as those in [4]–[30]. Absorptive filters using all-pass-type networks for in-parallel cascaded circuit arrangements were initially presented in [4]. To ensure even- and odd-mode subnetwork compensation in symmetrical circuit topologies (i.e., even- and odd-mode input reflection coefficients equal in amplitude but opposite in phase) that allow the attainment of a theoretically perfect absorptive behavior, families of two-port-reflectionless BPFs in lumped element and transmission line (TL) realizations were subsequently explored in [5]–[7]. Besides, inspired by these absorptive filtering techniques for symmetrical circuit schemes, a quasi-reflectionless super-conducting BPF was developed in [8]. Similarly, based on two identical wideband back-to-back cascaded quadrature couplers arranged in a two-branch/balanced circuit, a class of tunable two-port-reflectionless single-/dual-band BPFs and diplexers were reported in [9]. Alternatively, as another design method, complementary diplexer-based circuit architectures composed of shunt-connected bandpass and resistively

terminated bandstop channels were used in [10]–[16] to develop input- and two-port-quasi-reflectionless single-/dual-band BPFs, balanced BPFs, frequency-adaptive BPFs, and diplexers. At the same time, by optimizing the matching response of the lossy bandstop-type absorptive branches under this design philosophy, input-quasi-reflectionless BPFs and filtering couplers with extended upper stopband were discussed in [17]–[19]. Afterward, using lossy microstrip stubs as dissipative matching stages and lossy output isolation networks, input-absorptive reconfigurable BPFs and output-reflectionless filtering power dividers were, respectively, designed in [20] and [21]. Meanwhile, quasi-reflectionless single- and multiband BPFs can also be realized with lossy signal interference transversal filtering sections as reported in [22] and [23]. In addition, high-order quasi-absorptive BPFs with lossy stub-loaded parallel coupled-line circuit structures were presented in [24] for low-order designs, and subsequently extrapolated to higher selectivity filter realizations in [25]. More recently, by co-integrating wideband microstrip-to-microstrip vertical transition networks and shunt/in-series resistively terminated microstrip lines, two-port-reflectionless broadband BPFs and input-reflectionless wideband balun were conceived in [26] and [27], respectively. However, most of the aforementioned RF reflectionless filtering components are restricted to narrow or moderate bandwidth transfer functions, and only some of them (e.g., those in [6], [14], [25], and [29]) feature quasi-elliptic-type (QET) filtering responses. Meanwhile, they all exhibit one or several of the following drawbacks as undesired characteristics: 1) poor filtering selectivity and/or power-matching levels within limited absorptive frequency regions, 2) degraded passband amplitude flatness and power absorption ratio levels/profile within the stopband ranges and passband-to-stopband transitions, and 3) unproven applicability to multiport circuits. On the other hand, although various research works on wideband BPFs and filtering devices with QET responses have been conducted, such as those in [31]–[35], these circuits only present a reflective-type nature. Hence, their extension to properly engineered filtering circuit counterparts with broadband reflectionless behavior must still be addressed.

In this article, based on the previous research works on two-port-reflectionless wideband BPFs in [26] and the input-reflectionless lowpass filter (LPF) in [28], a class of input-reflectionless broadband filtering devices (i.e., BPFs and balun BPF) with QET responses in diplexer-based structures are theoretically proposed to achieve further improved passband amplitude flatness and sharper power absorption ratio profiles within the stopband-to-passband transitions. For illustration purposes, the generalized complementary diplexer network of the suggested BPF is shown in Fig. 1(a). Here, the wideband bandstop filter (BSF) channel is terminated by a 50-Ω port impedance (Z_0) to attain the expected QET transfer function with broadband input-reflectionless behavior. For an ideal input-reflectionless property, $Y_{\mathrm{BPF}}(f) + Y_{\mathrm{BSF}}(f) = Y_0$ must be perfectly satisfied where $Y_{\mathrm{BPF}}(f)$ and $Y_{\mathrm{BSF}}(f)$ are the admittances of the BPF and BSF channels, respectively. The expected conceptual power absorption ratio profile by exploiting the design of the proposed high-order wideband

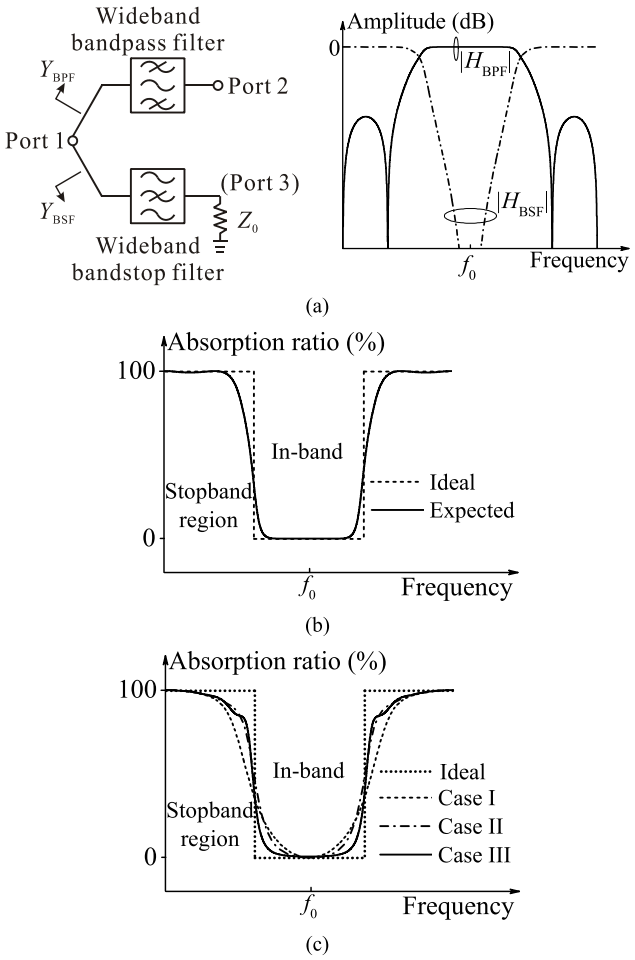

Fig. 1. Conceptual input-reflectionless diplexer-based wideband BPF with QET response and associated power absorption ratios (f_0 is the passband center frequency). (a) Generalized input-reflectionless diplexer-based wideband BPF network and desired QET BPF (H_{BPF}) and BSF (H_{BSF}) transfer functions. (b) Conceptual power absorption ratios (ideal profile and expected profile for this work) for the input-reflectionless QET wideband BPF. (c) Theoretical power absorption ratios of the two-port-reflectionless wideband BPFs reported in [26] that were designed with shunt/in-series resistively terminated one-section (Case I), three-section (Case II), and five-section (Case III) microstrip lines, respectively.

BPF is plotted in Fig. 1(b), which is intended to be as close as possible to the ideal one. In addition, the three sets of theoretical power absorption ratios corresponding to the wideband BPFs reported in [26] are also illustrated in Fig. 1(c) for comparison purposes, which are far from the ideal one. Here, it should be highlighted that although the wideband BPFs using shunt/in-series resistively terminated multisection microstrip lines presented in [26] were designed with two-port broadband reflectionless behavior, they suffered from degraded passband amplitude flatness, rounded power absorption ratio profiles within the stopband-to-passband transitions, and relatively poor filtering selectivity. Such shortcomings are also shared by the input-reflectionless balanced wideband BPF with QET response initially reported in [30], from which this article is an expanded version.

In this context, the frequency responses of the proposed wideband BPFs and balun BPF are specifically determined, which are intended to exhibit the following desired

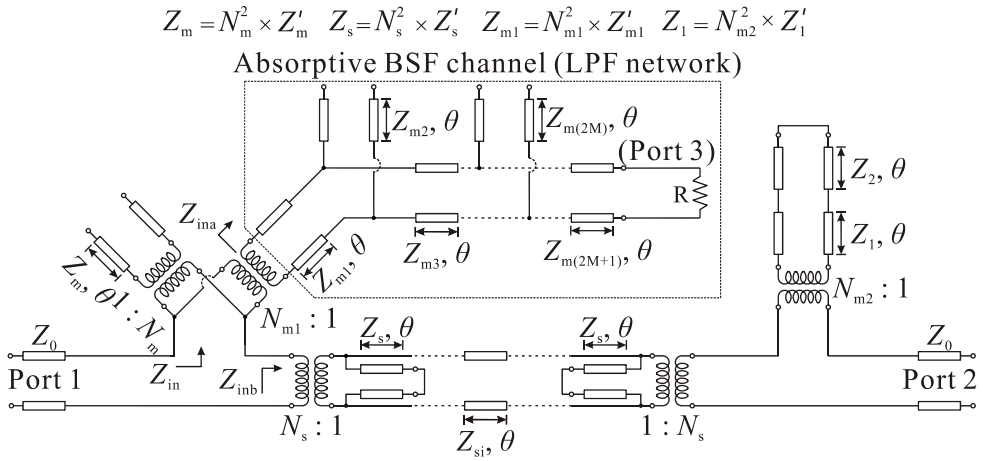

Fig. 2. Generalized diplexer-based TL equivalent circuit of the proposed class of input-reflectionless $(i+3)$th-order QET wideband BPFs using two parts: 1) a broadband microstrip-to-microstrip vertical transition modified with an in-series short-circuit-ended two-section microstrip line and 2) a shunt resistively terminated LPF network made up of hybrid multisection microstrip lines and open-circuit-ended microstrip stubs.

properties to overcome the aforementioned limitations: 1) two-/three-port high-order QET filtering responses based on microstrip-to-microstrip vertical transition networks modified with cascaded short-circuit-ended two-section microstrip lines or shunt open-circuit-ended half-wavelength microstrip stubs and 2) enhanced passband amplitude flatness and highly improved stopband power absorption ratio levels using a shunt resistively terminated high-order LPF network. Meanwhile, the RF operational principles and the theoretical foundations of these proposed filtering devices are detailed by the presented design procedures, for which the impedance values of their corresponding design parameters can be synthetically obtained by attaining the specified reflective-type Chebyshev in-band equal-ripple responses in their constituent BPF and resistively terminated BSF channels, simultaneously. To the best of the authors' knowledge, this is the first time that reflectionless wideband filtering circuits are synthetically designed. For practical validation purposes, four microstrip prototypes corresponding to three 2-GHz wideband BPFs and one 1-GHz broadband balun BPF in a two-layer substrate are designed, manufactured, and experimentally characterized.

The rest of this article is organized as follows. In Section II, third-order input-reflectionless QET wideband BPFs using a shunt resistively terminated microstrip T-junction and a π-shape structure are first presented. Subsequently, a higher order broadband BPF with highly increased out-of-band power attenuation levels is proposed by means of two in-series cascaded replicas of the third-order BPF using a shunt resistively terminated microstrip T-junction. Next, their application to a fourth-order input-reflectionless wideband balun BPF with QET response is reported in Section III. The comparison between the developed input-reflectionless broadband filtering prototypes and other prior art reflectionless wideband BPFs and balun BPFs is given in Section IV. Finally, the concluding remarks of this work are provided in Section V.

II. QET Wideband BPFs With Shunt Resistively Terminated LPF Networks

The generalized equivalent circuit of the proposed class of input-reflectionless diplexer-based wideband BPFs is depicted in Fig. 2. As shown, it consists of two signal transmission parts, as follows: 1) a BPF channel shaped by a reflective-type $(i+3)$th-order ($i = 0, 1, 2, \ldots$) microstrip-to-microstrip vertical transition network [36] modified with a cascaded ith-order TL section between two short-circuit-ended stubs and a short-circuit-ended two-section TL at the output port (Port 2) to realize a QET broadband filtering response and 2) a BSF channel built with a shunt resistively terminated LPF network. The LPF is composed of $M+1$ in-series cascaded TL sections ($M = 1, 2, 3, \ldots$) and M open-circuit-ended stubs with a resistor R loaded at the output port (Port 3). This resistively loaded LPF block operates as an absorptive lossy network to dissipate the out-of-band RF input signal energy reflected by the BPF channel so as to attain an overall broadband input-reflectionless behavior. The open-circuit-ended stub, the short-circuit-ended stubs, and the cascaded ith-order and short-circuit-ended two-stage TL sections of the reflective-type BPF channel, as well as the $M+1$ in-series cascaded TL sections and the M open-circuit-ended stubs of the absorptive LPF, are designed with the same electrical length $\theta = \pi/2$ at f_0 (i.e., quarter-wavelength TL segments at f_0) but with different characteristic impedances (Z_m, Z_s, $Z_{s1}, \ldots, Z_{si}$, Z_1, Z_2, Z_{m1}, $Z_{m3}, \ldots, Z_{m(2M+1)}$, and $Z_{m2}, \ldots, Z_{m(2M)}$). Meanwhile, R is the resistance of the loading resistor, and Z_{in}, $Z_{\text{in}a}$, and $Z_{\text{in}b}$ represent the input impedances of the relevant TL structures. In addition, due to the open-/short-circuit-ended and coupling effects in the circuit electromagnetic (EM) simulation and measurement, four transformers with different turns ratios of N_m, N_s, N_{m1}, and N_{m2} are used to model the impedance variations in the coupled microstrip lines/sections and the slotline resonator.

In the following, a third-order QET wideband BPF with enhanced passband amplitude flatness and improved stopband power absorption-ratio levels is first presented using a resistively terminated microstrip T-junction with $M = 1$. Then, its counterpart on a resistively terminated π-shape LPF network with $M = 2$ is proposed to demonstrate further improved stopband power absorption ratio levels. Afterward, to attain even higher stopband power attenuation levels and enhanced sharpness for the power absorption ratio profile

within the stopband-to-passband transitions when compared with the third-order BPFs, a higher order BPF using two in-series cascaded replicas of the third-order BPF unit on the resistively terminated microstrip T-junction is reported. Moreover, as can be deduced from Fig. 1(a), although the perfect design condition for the proposed input-reflectionless diplexer-based BPFs can be mathematically expressed as

$$Y_0 = Y_{\mathrm{BPF}}(f) + Y_{\mathrm{BSF}}(f) \;\Rightarrow |S_{11}| \to -\infty \text{ dB} \tag{1}$$

such ideal design requisite is unfeasible in a practical design. Hence, minimum in-band power-matching levels above or around 20 dB for the constituent quasi-complementary BPF and BSF channels of the BPFs and balun BPF of this work are theoretically imposed. Thus, $|S_{11}| \leq -20$ dB or return loss (RL) $\geq$20 dB can be attained for the complete filtering devices throughout a broad input-quasi-reflectionless spectral range.

A. Third-Order Wideband BPF on a Resistively Terminated Microstrip T-Junction With $i = 0$ and $M = 1$

The suggested input-reflectionless BPF shaped by a third-order QET wideband vertical transition network with $i = 0$ and a resistively terminated TL T-junction with $M = 1$ is analyzed as lossless network with $N_m = N_s = N_{m1} = N_{m2} = 1$. Initially, the frequency response of the reflective-type BPF channel is discussed. With the derived *ABCD* matrix of the built circuit network for $i = 0$, the formulas for the squared power transmission (S_{21}) and reflection (S_{11}) parameters in amplitude depending on the characteristic function F_{M} are determined as

$$|S_{21}|^2 = \frac{1}{1+|F_{\mathrm{M}}|^2} \;\&\; |S_{11}|^2 = \frac{|F_{\mathrm{M}}|^2}{1+|F_{\mathrm{M}}|^2} \tag{2}$$

$$F_{\mathrm{M}} = \frac{(A-D)+(B-C)}{2} \tag{3}$$

where

$$A - D = -\frac{2z_m}{z_s \tan^2\theta} - \frac{2z_1(z_1+z_2)}{z_s(z_1 - z_2\tan^2\theta)} \tag{4a}$$

$$B - C = j\left(-\frac{z_m}{\tan\theta} + \frac{z_1(z_1+z_2)(z_s\tan^2\theta - 2z_m)\tan\theta}{z_s(z_1 - z_2\tan^2\theta)\tan^2\theta} + \frac{2}{z_s\tan\theta}\right) \tag{4b}$$

and z_m, z_s, z_1, and z_2 are the normalized impedances. To realize a three-pole QET Chebyshev equal-ripple response, the real part of F_{M} is forced to be equal to zero by imposing A-D = 0, so that

$$\tan^2\theta = \frac{z_m z_1}{z_m z_2 - z_1(z_1+z_2)} \;\&\; z_m > \frac{z_1(z_1+z_2)}{z_2}. \tag{5}$$

From (5), it is found that besides the inherent transmission pole at f_0, two additional in-band transmission poles at f_{TP1} and f_{TP2} are generated as follows:

$$f_{\mathrm{TP1}} = \frac{2f_0}{\pi}\tan^{-1}\sqrt{\frac{z_m z_1}{z_m z_2 - z_1(z_1+z_2)}} \tag{6a}$$

$$f_{\mathrm{TP2}} = 2f_0\left(1 - \frac{1}{\pi}\tan^{-1}\sqrt{\frac{z_m z_1}{z_m z_2 - z_1(z_1+z_2)}}\right). \tag{6b}$$

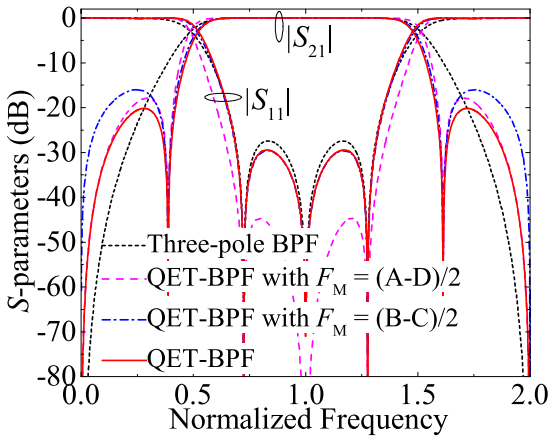

Fig. 3. Theoretical power transmission ($|S_{21}|$) and reflection ($|S_{11}|$) responses of the third-order reflective-type wideband QET BPF channel of the proposed wideband BPF ($Z_0 = 50\ \Omega$) without considering the absorptive LPF network for $i = 0$ and $M = 1$ when $z_m = 1.122$, $z_s = 1.1319$, $z_1 = 0.6768$, and $z_2 = 1.3947$.

From (6a) and (6b), the fractional bandwidth (FBW) between these two transmission poles can be defined as

$$\mathrm{FBW_{TP}} = 2f_0 - \frac{4f_0}{\pi}\tan^{-1}\sqrt{\frac{z_m z_1}{z_m z_2 - z_1(z_1+z_2)}}. \tag{7}$$

Meanwhile, in addition to the intrinsic power transmission zeros (TZs) that are located at 0 and $2f_0$ for which $|S_{21}| = 0$, two more real-frequency TZs are produced by the short-circuit-ended two-section TL. Their locations at f_{TZ1} and f_{TZ2} are given below:

$$f_{\mathrm{TZ1}} = \frac{2f_0}{\pi}\tan^{-1}\sqrt{\frac{z_1}{z_2}} \tag{8a}$$

$$f_{\mathrm{TZ2}} = 2f_0\left(1 - \frac{1}{\pi}\tan^{-1}\sqrt{\frac{z_1}{z_2}}\right). \tag{8b}$$

Hence, by mathematically making $\mathrm{FBW_{TP}}$ of this QET BPF channel equal to the one derived for the three-pole wideband vertical transition as reported in [36], it results in

$$\frac{z_1}{z_m z_2 - z_1(z_1+z_2)} = \frac{z_m}{z_m z_s - 1}. \tag{9}$$

With (9) and the real-frequency TZs at f_{TZ1} and f_{TZ2} determined by the specified impedance ratio $R_Z = z_1/z_2$, the values for the normalized impedances z_m, z_s, z_1, and z_2 of the reflective-type QET BPF channel with Chebyshev equal-ripple response are derived from the predefined in-band ripple-level factor L_{A1} and electrical length θ_{c1} at the lower cutoff frequency. As an illustrative example, the theoretical frequency response of the proposed BPF channel with the third-order QET Chebyshev equal-ripple behavior is depicted in Fig. 3. Here, by selecting $L_{\mathrm{A1}} = 0.0078$ and $\theta_{\mathrm{c1}} = 61.92°$, a three-pole Chebyshev equal-ripple response with $\mathrm{FBW_{TP}}$ of 55.2% resulting from $z_m = 1.122$ and $z_s = 1.1319$ [36] is initially obtained. With (9) and $R_z = 0.4853$, the third-order QET Chebyshev equal-ripple response of the BPF channel with the same $\mathrm{FBW_{TP}}$ is then determined for $z_1 = 0.6768$ and $z_2 = 1.3947$. As shown, both the frequency responses of the BPF channel associated with the real and imaginary

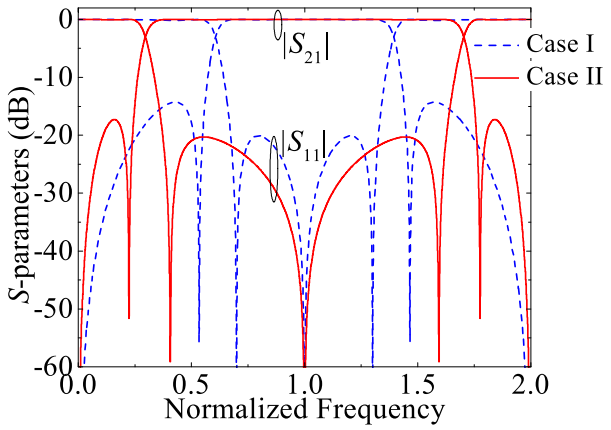

Fig. 4. Analyses of the locations of the real-frequency TZs at f_{TZ1} and f_{TZ2} of the third-order reflective-type wideband QET BPF channel with the possible smallest and largest FBWs in a practical design by considering the design condition RL $\geq$ 20 dB (Case I: $z_m = 1.644$, $z_s = 1.0381$, $z_1 = 0.496$, and $z_2 = 0.4$; Case II: $z_m = 0.602$, $z_s = 2.7539$, $z_1 = 0.4$, and $z_2 = 2.9561$).

parts of its F_{M} characteristic function exhibit QET Chebyshev equal-ripple performance with the same $\mathrm{FBW_{TP}}$, but different RL levels. It should also be noted that although the in-band ripple-level constant of the proposed QET BPF differs from the predefined L_{A1}, its power-matching level satisfies the prefixed condition $|S_{11}| \leq -20$ dB under which the slight difference in terms of FBWs between the proposed QET BPF and the three-pole BPF determined by L_{A1} and θ_{c1} can be ignored. Besides, by considering manufacturing tolerances and a specific microstrip substrate, analyses about the practically feasible frequency locations for the two real-frequency TZs at f_{TZ1} and f_{TZ2} have been conducted. Herein, a Rogers 4003C substrate with relative dielectric constant $\varepsilon_{\mathrm{r}} = 3.55$, dielectric thickness $h = 0.813$ mm, metal thickness $t = 35$ μm, and dielectric loss tangent $\tan(\delta_{\mathrm{D}}) = 0.0027$ is used for the three BPF circuits in this section. Due to the 0.1-mm tolerance, the end effect of the microstrip line and the slotline resonator as in [37], the minimum impedance values of the microstrip lines and slotline resonator for the practical design are chosen as 20 and 51.904 Ω, whereas the maximum impedance values for them are selected as 147.804 and 137.695 Ω, respectively. Hence, based on the design condition $|S_{11}| \leq -20$ dB, the relevant frequency responses of the QET BPF channel designed with the possible smallest and largest FBWs (i.e., Case I and Case II) are depicted in Fig. 4. They reveal $0.224 \leq f_{\mathrm{TZ1}} \leq 0.534$, $1.466 \leq f_{\mathrm{TZ2}} \leq 1.776$, and $0.135 \leq R_z \leq 1.24$ as feasible ranges.

Next, the input-reflectionless property of the proposed overall QET BPF network with $i = 0$ and the shunt resistively terminated TL T-junction (i.e., $M = 1$) is properly analyzed. As shown in Fig. 2, the normalized input impedance $z_{\mathrm{in}a}$ of the resistively terminated T-junction with $R = Z_0$ is derived as

$$z_{\mathrm{in}a} = \frac{z_{m1}^2 z_{m2}^2 z_{m3}^2 (1+\tan^2\theta)^2 + ja}{b^2 + c^2} \tag{10}$$

where

$$\begin{aligned} a = {} & \left(z_{m1}^2 z_{m2}^2 z_{m3}^3 + z_{m1}^3 z_{m2}^2 z_{m3}^2 - z_{m1}^2 z_{m2}^2 z_{m3} - z_{m1}^2 z_{m2} z_{m3}^2 \right. \\ & \left. - z_{m1} z_{m2}^2 z_{m3}^2\right) \tan\theta - z_{m1}^3 z_{m2} z_{m3}^3 \tan^2\theta \\ & - \left(z_{m1}^2 z_{m2} z_{m3}^4 + z_{m1} z_{m2}^2 z_{m3}^4 + z_{m1}^3 z_{m2} z_{m3}^3 + z_{m1}^2 z_{m2}^2 z_{m3}^3 \right. \\ & - z_{m1}^3 z_{m2}^2 - 2 z_{m1}^3 z_{m2} z_{m3} - z_{m1}^2 z_{m2}^2 z_{m3} - z_{m1}^3 z_{m3}^2 \\ & \left. - z_{m1}^2 z_{m2} z_{m3}^2\right) \tan^3\theta + \left(z_{m1}^3 z_{m3}^4 + z_{m1}^2 z_{m2} z_{m3}^4\right) \tan^4\theta \end{aligned} \tag{11a}$$

$$b = z_{m1} z_{m2} z_{m3} - \left(z_{m1} z_{m3}^2 + z_{m2} z_{m3}^2\right) \tan^2\theta \tag{11b}$$

$$c = \left(z_{m1} z_{m2} + z_{m1} z_{m3} + z_{m3} z_{m3}\right) \tan\theta \tag{11c}$$

and z_{m1}, z_{m2}, and z_{m3} are the normalized impedances. From the above expression, it is obvious that $z_{\mathrm{in}a}$ is a complex-valued function, which results in a complex normalized z_{in} given by

$$z_{\mathrm{in}} = \frac{z_m z_{\mathrm{in}a}}{z_m + j z_{\mathrm{in}a} \tan\theta}. \tag{12}$$

With (10)–(12), the *ABCD* elements of the conceived whole input-reflectionless diplexer-based lossy BPF network can be formulated as follows:

$$\begin{aligned} A_1 &= 1 - \frac{2jz_{\mathrm{in}}}{z_s \tan\theta} \quad B_1 = z_{\mathrm{in}} + \frac{j z_1 (z_1 + z_2) \tan\theta}{z_1 - z_2 \tan^2\theta} \\ &\quad \times \left(1 - \frac{2jz_{\mathrm{in}}}{z_s \tan\theta}\right) \\ C_1 &= \frac{-2j}{z_s \tan\theta} \quad D_1 = 1 + \frac{2z_1(z_1+z_2)}{z_s(z_1 - z_2\tan^2\theta)}. \end{aligned} \tag{13}$$

To theoretically determine z_m, z_s, z_1, z_2, z_{m1}, z_{m2}, and z_{m3}, by adopting an analogous procedure as in the previous case, $A_1 - D_1 = 0$ is imposed so that the characteristic function of this input-reflectionless BPF network is $F_{\mathrm{M1}} = (B_1 - C_1)/2$ with $z_{\mathrm{in}a} = ja/(b^2 + c^2)$. Then, the FBW_{TP} parameter of the reflective-type QET Chebyshev equal-ripple response is forced to be equal to the one derived for the specified L_{A1} and θ_{c1} for the vertical transition as in [36]. With (9) and the desired R_z, the initial set of z_m, z_s, z_1, and z_2 can be obtained. Then, to calculate z_{m1}, z_{m2}, and z_{m3}, it is supposed that the output port (Port 2) of the reflective-type BPF channel is terminated by a 50-Ω port impedance, whereas the resistor R at the output port (Port 3) of the BSF channel is removed. Hence, the *ABCD* elements of the reshaped lossy BSF channel, which is actually an input-reflectionless fifth-order LPF, can be expressed as follows:

$$\begin{aligned} A_2 = {} & \cos^2\theta + j\left(\frac{z_{\mathrm{in}b}}{z_{m1}} + \frac{z_{\mathrm{in}b}}{z_{m2}} + \frac{z_{\mathrm{in}b}}{z_{m3}}\right) \sin\theta\cos\theta \\ & - \left(\frac{z_{m1}}{z_{m2}} + \frac{z_{m1}}{z_{m3}}\right) \sin^2\theta - j\left(\frac{z_{\mathrm{in}b} z_{m1}}{z_m z_{m2}} + \frac{z_{\mathrm{in}bn} z_{m1}}{z_m z_{m3}}\right) \\ & \times \sin^2\theta \tan\theta + j\frac{z_{\mathrm{in}bnn}}{z_m} \cos^2\theta \tan\theta \end{aligned} \tag{14a}$$

$$\begin{aligned} B_2 = {} & z_{\mathrm{in}b} \cos^2\theta + j(z_{m1} + z_{m3}) \sin\theta\cos\theta \\ & - \left(\frac{z_{\mathrm{in}b} z_{m1}}{z_m} + \frac{z_{\mathrm{in}b} z_{m3}}{z_m} + \frac{z_{\mathrm{in}b} z_{m3}}{z_{m1}} + \frac{z_{\mathrm{in}b} z_{m3}}{z_{m2}}\right) \sin^2\theta \\ & - j\frac{z_{m1} z_{m3}}{z_{m2}} \sin^2\theta \tan\theta + \frac{z_{\mathrm{in}b} z_{m1} z_{m3}}{z_m z_{m2}} \sin^2\theta \tan^2\theta \end{aligned} \tag{14b}$$

$$\begin{aligned} C_2 = {} & j\left(\frac{1}{z_m} + \frac{1}{z_{m1}} + \frac{1}{z_{m2}} + \frac{1}{z_{m3}}\right) \sin\theta\cos\theta \\ & - j\left(\frac{z_{m1}}{z_m z_{m2}} + \frac{z_{m1}}{z_m z_{m3}}\right) \sin^2\theta \tan\theta \end{aligned} \tag{14c}$$

$$D_2 = \cos^2\theta - \left(\frac{z_{m1}+z_{m3}}{z_m} + \frac{z_{m3}}{z_{m1}} + \frac{z_{m3}}{z_{m2}}\right)\sin^2\theta + \frac{z_{m1}z_{m3}}{z_m z_{m2}}\sin^2\theta\tan^2\theta \quad (14d)$$

where $z_{\text{in}b}$ is the normalized input impedance given by

$$z_{\text{in}b} = \frac{\tan^2\theta z_s^2(z_1 - z_2\tan^2\theta)^2 + ja_1}{b_1^2 + c_1^2} \quad (15)$$

with

$$a_1 = 2z_s\tan\theta(z_1 - z_2\tan^2\theta)^2 + z_1z_s(z_1+z_2) \times (2z_1(z_1+z_2) + z_s(z_1 - z_2\tan^2\theta))\tan^3\theta \quad (16a)$$

$$b_1 = 2(z_1 - z_2\tan^2\theta) \quad (16b)$$

$$c_1 = 2z_1(z_1+z_2) + z_s(z_1 - z_2\tan^2\theta). \quad (16c)$$

Similarly, by designing the reflective-type LPF response of this reshaped BSF channel with Chebyshev LPF polynomials, the original set of z_{m1}, z_{m2}, and z_{m3} can be extracted. Here, the Chebyshev LPF polynomial function [38] is formulated as

$$|S_{21}(\theta)|^2 = \frac{1}{1+\varepsilon^2\cos^2(n\varphi + q\xi)} \quad (17)$$

where

$$\varepsilon = \sqrt{10^{0.1L_{A2}} - 1} \quad (18a)$$

$$\cos\varphi = \alpha x \ \ \& \ \ \cos\xi = \cos\varphi\sqrt{\frac{\alpha^2-1}{\alpha^2 - \cos^2\varphi}} \quad (18b)$$

and $x = \sin(\theta)$, $x_c = 1/\sin(\theta_{c2})$, ε is the specified in-band equal-ripple constant, L_{A2} is the ripple-level factor, and θ_{c2} is the relevant electrical length at the lower cutoff frequency. In addition, n represents the number of the cascaded TL sections and q is the order of the power TZs, which is related to the number of used shunt open-circuit-ended stubs. To realize a fifth-order Chebyshev equal-ripple LPF response for the reshaped lossy LPF network with the assumed $F_{M2} = (B_2 - C_2)/2$ and $z_{\text{in}b} = ja_1/(b_1^2 + c_1^2)$, $n = 3$ and $q = 2$ are selected. For this case, the theoretical function F_{the} results to be as follows:

$$F_{the} = k_1\frac{\sin\theta}{\cos^2\theta} + k_2\frac{\sin^3\theta}{\cos^2\theta} + k_3\frac{\sin^5\theta}{\cos^2\theta} \quad (19)$$

where

$$k_1 = \varepsilon(3\alpha + 2\sqrt{\alpha^2-1}) \quad (20a)$$

$$k_2 = -\varepsilon(10\alpha^3 + 10\alpha^2\sqrt{\alpha^2-1} - 3\alpha) \quad (20b)$$

$$k_3 = \varepsilon(8\alpha^5 + 8\alpha^4\sqrt{\alpha^2-1} - 4\alpha^3). \quad (20c)$$

With (19) and (20), the specific L_{A2} and θ_{c2}, and the relevantly derived characteristic function associated with a reflective-type fifth-order symmetrical LPF network [39], a reference set of z_{m1}, z_{m2}, and z_{m3} can be extracted. Subsequently, the determination of the impedance values of the proposed input-reflectionless BPF is quantitatively performed. With the specific $L_{A1} = 0.02075$, $\theta_{c1} = 57.118°$, $R_z = 0.5212$, and (9), $z_m = 1.1273$, $z_s = 1.2404$, $z_1 = 0.62$, and $z_2 = 1.1896$ are first obtained. This results in a reflective-type QET Chebyshev filtering response on (2)–(4), as presented in Fig. 5(a). Meanwhile, with the assumed $L_{A2} = 0.001251$, $\theta_{c2} = 47.61°$,

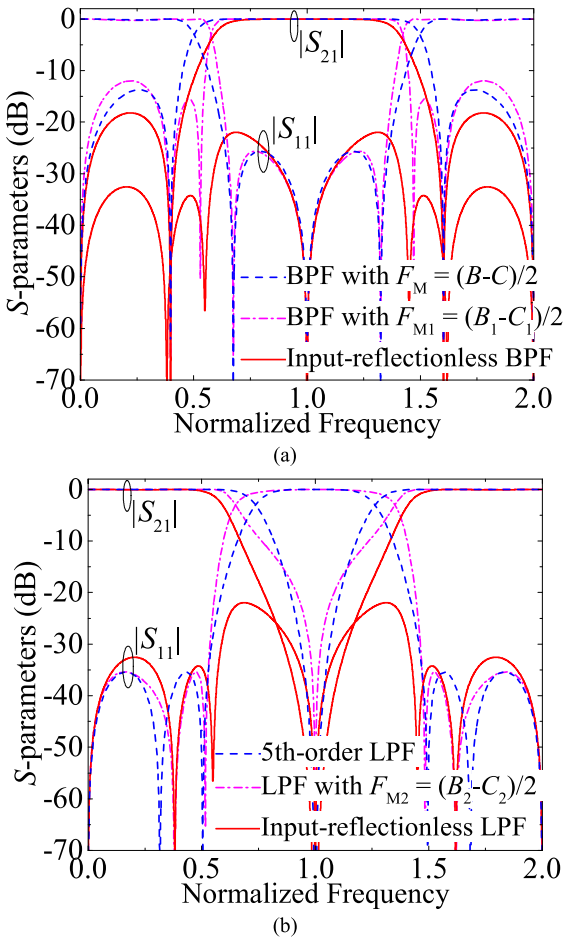

Fig. 5. Theoretical power transmission ($|S_{21}|$) and input reflection ($|S_{11}|$) responses of the diplexer-based input-reflectionless three-pole BPF and the reshaped fifth-order lossy LPF with $z_m = 0.9002$, $z_s = 1.1559$, $z_1 = 0.7926$, $z_2 = 1.5207$, $z_{m1} = 1.8129$, $z_{m2} = 1.3466$, and $z_{m3} = 1.1298$. (a) Frequency responses of the proposed input-reflectionless BPF. (b) Frequency responses of the reshaped lossy LPF network.

(19), and (20), then the values $z_{m1} = 1.1147$, $z_{m2} = 1.748$, and $z_{m3} = 0.62$ for a reflective-type symmetrical fifth-order LPF as shown in Fig. 5(b) are derived. With these initially determined impedance values, quantitative tuning procedures are carried out to simultaneously attain the specific QET Chebyshev in-band response for the input-reflectionless lossy BPF with $F_{M1} = (B_1 - C_1)/2$ and $z_{\text{in}a} = ja/(b^2 + c^2)$ and the precise Chebyshev fifth-order in-band LPF response for the reshaped lossy LPF with $F_{M2} = (B_2 - C_2)/2$ and $z_{\text{in}b} = ja_1/(b_1^2 + c_1^2)$. As shown in Fig. 5(a) and (b), these two reflective-type Chebyshev equal-ripple BPF and LPF responses are obtained for $z_m = 0.9002$, $z_s = 1.1559$, $z_1 = 0.7926$, $z_2 = 1.5207$, $z_{m1} = 1.8129$, $z_{m2} = 1.3466$, and $z_{m3} = 1.1298$, which also gives rise to the desired input-reflectionless BPF and LPF responses at the same time.

For experimental validation purposes, a proof-of-concept prototype of this input-reflectionless wideband BPF with $i = 0$ and $M = 1$ is designed, manufactured, and tested. Fig. 6 shows the 3-D layout of the developed wideband BPF circuit that was implemented in a two-layered structure. Here, the open-circuit-ended stub, the short-circuit-ended stubs, the short-circuit-ended two-section TL, and the shunt resistively

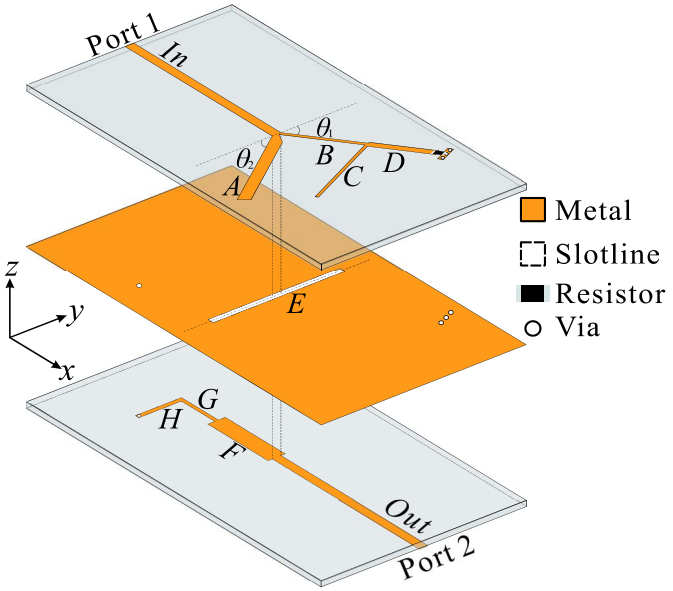

Fig. 6. 3-D layout of the developed input-reflectionless QET wideband BPF prototype using a shunt resistively terminated microstrip T-junction for $i = 0$ and $M = 1$ ($L_{\rm In} = L_{\rm Out} = 52$, $L_{\rm A} = 21.25$, $L_{\rm B} = 23.45$, $L_{\rm C} = 22.87$, $L_{\rm D} = 22.65$, $L_{\rm E} = 49.46$, $L_{\rm F} = 21.59$, $L_{\rm G} = 12$, $L_{\rm H} = 11.3$, $W_{\rm In} = W_{\rm Out} = 1.82$, $W_{\rm A} = 2.42$, $W_{\rm B} = 0.54$, $W_{\rm C} = 1.3$, $W_{\rm D} = 1.6$, $W_{\rm E} = 0.24$, $W_{\rm F} = 2.86$, $W_{\rm G} = W_{\rm H} = 0.96$ (unit: mm), $\theta_1 = 75°$, and $\theta_2 = 30°$).

terminated T-junction shown in Fig. 2 are represented by an open-circuit-ended microstrip resonator, slotlines, short-circuit-ended two-cascaded microstrip sections, and a shunt microstrip T-junction, respectively. Additionally, the short-circuit-ended in-series microstrip sections are arranged in a folded structure for a compact circuit size. Based on the obtained normalized impedances, this input-reflectionless wideband BPF centered at $f_0 = 2$ GHz is designed with $Z_m = 45.0114\ \Omega$, $Z_s = 57.7969\ \Omega$, $Z_1 = 39.6298\ \Omega$, $Z_2 = 76.0365\ \Omega$, $Z_{m1} = 90.6474\ \Omega$, $Z_{m2} = 67.3283\ \Omega$, $Z_{m3} = 56.4916\ \Omega$, and $R = 50\ \Omega$. However, due to the existing coupling and open-/short-circuit-ended effects during the EM simulation via Ansys HFSS software, the designed wideband BPF is simulated with $Z'_{\rm m} = 41.06\ \Omega$, $Z'_{\rm s} = 83.595\ \Omega$, $Z'_1 = 36.64\ \Omega$, $Z_2 = 70.303\ \Omega$, $Z'_{\rm m1} = 90.34\ \Omega$, $Z_{m2} = 67.1\ \Omega$, and $Z_{m3} = 56.3\ \Omega$ to make the EM-simulated results fairly close to the theoretical ones. Hence, based on these two sets of impedance values, the turns ratios of the transformers are extracted as $N_m = 1.047$, $N_s = 0.8315$, $N_{m1} = 1.0017$, and $N_{m2} = 1.04$. Meanwhile, a surface-mounted device (SMD) resistor with measured resistance $R = 50.2\ \Omega$ is used in the absorptive LPF branch.

The theoretical, EM-simulated, circuit model, and measured power transmission and input reflection responses of the manufactured wideband BPF prototype are depicted in Fig. 7(a). As shown, a QET wideband filtering response with remarkable passband flatness and broadband input-reflectionless behavior is measured, being in fairly close agreement with the theoretical and simulated results. The wideband BPF prototype is measured with a center frequency of 2.004 GHz, a minimum in-band power insertion loss level of 0.37 dB, 1-, and 3-dB FBWs of 71.08% and 86.78%, respectively (i.e., passband flatness factor of 81.91% as defined in [26]), a minimum stopband power rejection level of 13.7 dB, and input power-matching

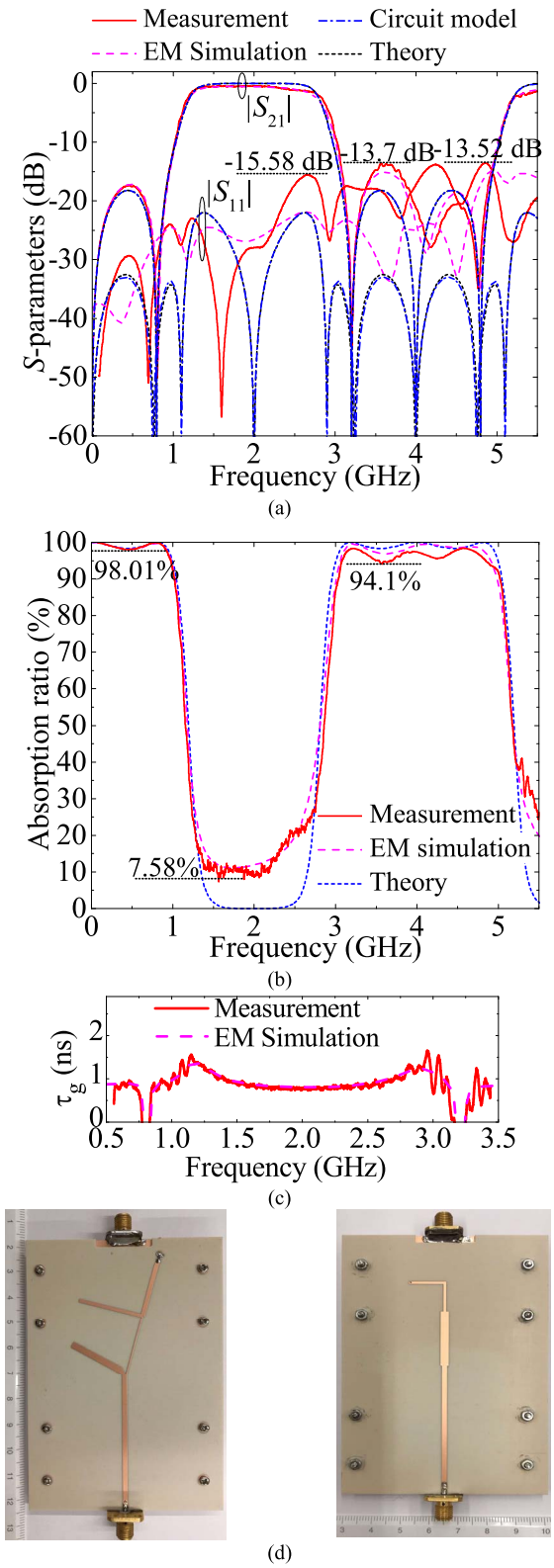

Fig. 7. Frequency responses of the manufactured input-reflectionless QET wideband BPF prototype shown in Fig. 6. (a) Theoretical, EM-simulated, circuit model, and measured power transmission ($|S_{21}|$) and input-reflection ($|S_{11}|$) responses. (b) Theoretical, simulated, and measured power absorption ratios [i.e., $100\times(1-|S_{21}|^2-|S_{11}|^2)$ (%)]. (c) Simulated and measured in-band group delay ($\tau_{\rm g}$) responses. (d) Photograph (top/bottom view) of the assembled BPF prototype.

levels above 13.52 dB in the entire represented frequency range. Fig. 7(b) plots the theoretical, simulated, and measured

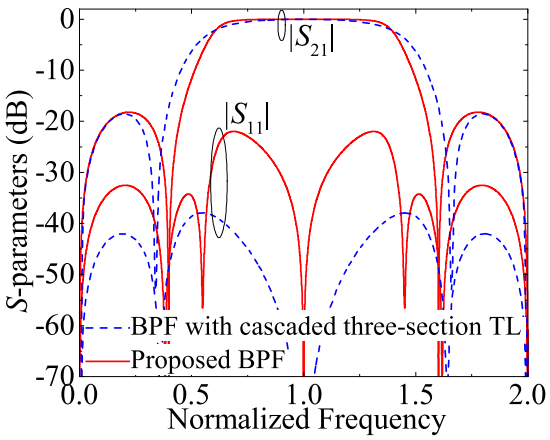

Fig. 8. Theoretical power transmission ($|S_{21}|$) and input reflection ($|S_{11}|$) responses of the proposed input-reflectionless QET wideband BPFs designed with the discussed shunt resistively terminated LPF T-junction and a shunt resistively terminated three-section TL reported in [26], respectively.

power absorption ratios. Compared with the theoretical ones shown in Fig. 1(c) associated with the reflectionless wideband BPFs reported in [26], the stopband power absorption ratios and their sharpness at the stopband-to-passband transitions are highly improved so that the filter design principle is verified. Minimum stopband power absorption ratio levels above 94.1% from 0 to 4.89 GHz (i.e., without considering the passband range) and 7.58% at 1.87 GHz are measured. The maximum in-band group delay variation for this prototype, as inferred from the response in Fig. 7(c), is 0.82 ns. Fig. 7(d) depicts the top- and bottom-view photographs of the assembled wideband BPF prototype. Moreover, to further emphasize the efficacy of the used resistively terminated TL T-junction on improving the passband amplitude flatness, a comparison of the theoretical frequency responses for the proposed input-reflectionless diplexer-based BPFs designed with the discussed resistively ended LPF T-junction and the shunt resistively terminated three-section TL reported in [26], respectively, is illustrated in Fig. 8. Herein, the counterpart with the resistively ended three-section TL is designed with $z_m = 1.046$, $z_s = 1.114$, $z_1 = 0.55$, $z_2 = 1.568$, $z_{m1} = 1.316$, $z_{m2} = 0.936$, and $z_{m3} = 0.948$, for which z_{m1}, z_{m2}, and z_{m3} are assigned as the normalized impedances of the resistively terminated three-section TL. As can be seen, whereas QET wideband filtering responses with almost the same out-of-band power attenuation levels and higher power-matching levels for this BPF counterpart are obtained, the newly conceived input-reflectionless BPF with the resistively terminated T-junction exhibits superior passband amplitude flatness at the passband edges as one of the main design purposes of this work.

B. Third-Order Wideband BPF on a Resistively Terminated Microstrip π-Shape Structure With $i = 0$ and $M = 2$

As previously discussed, the used lossy BSF channel made up of a resistively terminated LPF T-junction in the conceived three-port diplexer-based network results in high selectivity and improved passband amplitude flatness for the overall BPF device. As such, the band-rounding effect of the two-port-reflectionless wideband BPFs reported in Section II-B

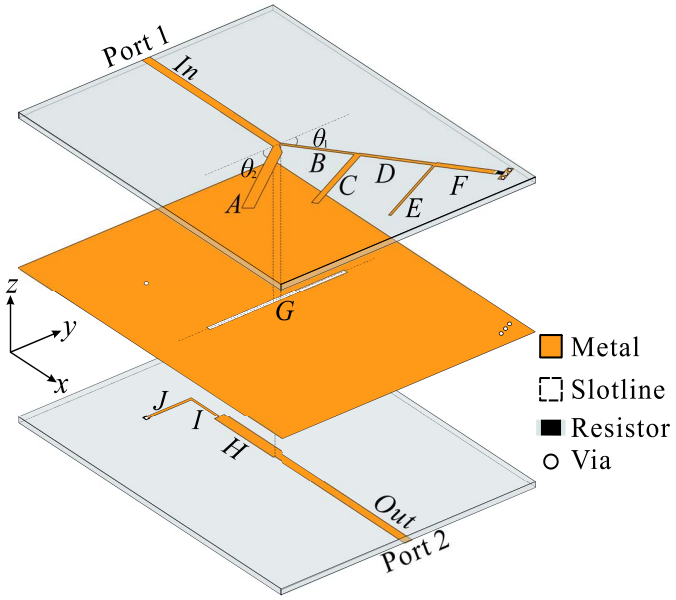

Fig. 9. 3-D layout of the developed input-reflectionless QET wideband BPF prototype using a shunt resistively terminated microstrip π-type structure for $i = 0$ and $M = 2$ ($L_{\rm In} = 52$, $L_{\rm Out} = 77$, $L_{\rm A} = 21.25$, $L_{\rm B} = 24$, $L_{\rm C} = 22.98$, $L_{\rm D} = 24.05$, $L_{\rm E} = 24.03$, $L_{\rm F} = 23.1$, $L_{\rm G} = 49.46$, $L_{\rm H} = 22$, $L_{\rm I} = 11.44$, $L_{\rm J} = 12.26$, $W_{\rm In} = W_{\rm Out} = 1.82$, $W_{\rm A} = 2.42$, $W_{\rm B} = 0.54$, $W_{\rm C} = 2.1$, $W_{\rm D} = 0.76$, $W_{\rm E} = 0.68$, $W_{\rm F} = 1.38$, $W_{\rm G} = 0.18$, $W_{\rm H} = 1.98$, $W_{\rm I} = W_{\rm J} = 0.24$ (unit: mm), $\theta_1 = 75°$, and $\theta_2 = 30°$).

of [26] is partially overcome here. Thus, it is expected that further increased levels of passband amplitude flatness and stopband power absorption ratio are feasible using a resistively terminated higher order LPF structure in the BSF channel. For verification purposes, an input-absorptive wideband BPF with $i = 0$ and $M = 2$ is subsequently addressed. Its BSF channel is designed as a resistively ended fifth-order LPF network in a TL π-shape structure. Thus, by terminating the output port (Port 2) of the reflective-type BPF channel of the whole diplexer-based BPF with a 50-Ω port impedance, the reshaped BSF operates as an input-reflectionless seventh-order lossy LPF circuit.

Following the same design procedure detailed in Section II-A, this proposed wideband input-reflectionless QET BPF with enhanced passband amplitude flatness and improved stopband power absorption ratio is finally designed with normalized impedances of $z_m = 0.886$, $z_s = 1.1126$, $z_1 = 0.936$, $z_2 = 2.4238$, $z_{m1} = 1.8619$, $z_{m2} = 0.8908$, $z_{m3} = 1.6318$, $z_{m4} = 16631$, $z_{m5} = 1.1165$, and $R = 50$ Ω. To experimentally validate the design expectations, a proof-of-concept prototype of the wideband BPF with the implemented two-layered circuit layout depicted in Fig. 9 is simulated and tested. This wideband BPF is simulated with $Z'_{\rm m} = 41.06$ Ω, $Z'_{\rm s} = 80.264$ Ω, $Z'_1 = 46.77$ Ω, $Z_2 = 121.744$ Ω, $Z'_{\rm m1} = 90.74$ Ω, $Z_{m2} = 44.541$ Ω, $Z_{m3} = 81.588$ Ω, $Z_{m4} = 83.156$ Ω, and $Z_{m5} = 55.824$ Ω. Thus, the turns ratios of the used transformers are determined as $N_m = 1.0387$, $N_s = 0.8325$, $N_{m1} = 1.0129$, and $N_{m2} = 1.0003$. The resistance of the SMD resistor soldered in the output port of the LPF network is measured as 50.3 Ω.

Fig. 10 depicts the frequency responses and the top-/bottom-view photographs of the assembled wideband

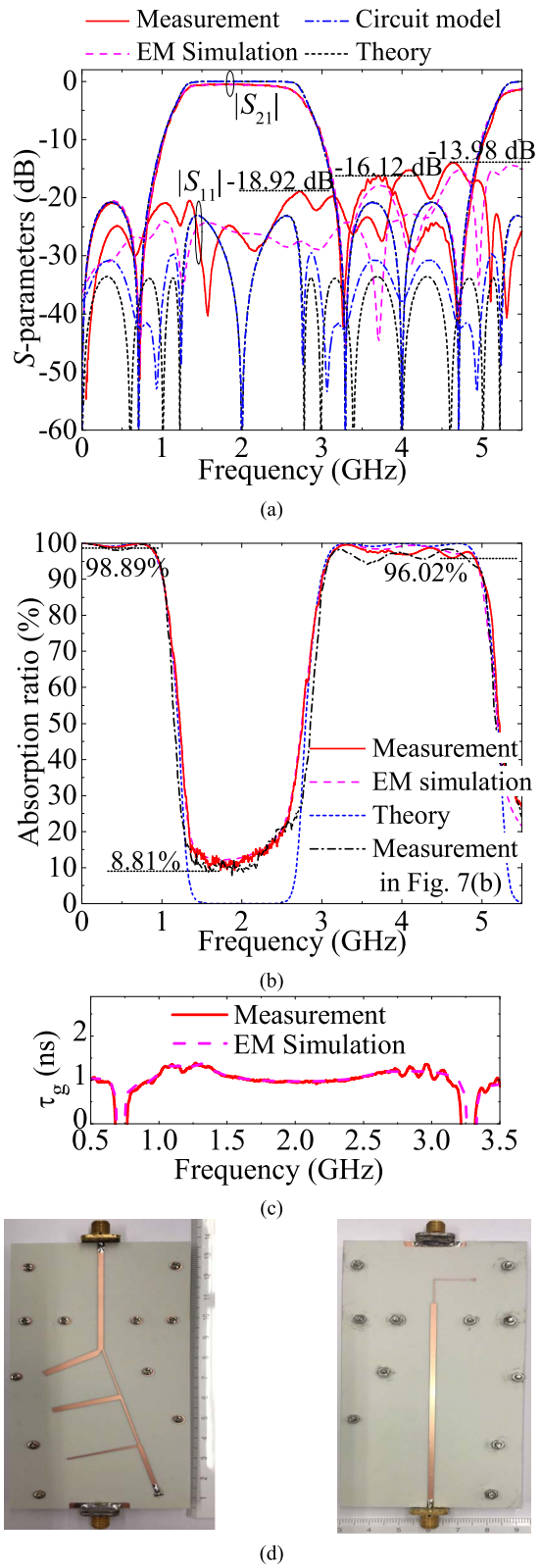

Fig. 10. Frequency responses of the manufactured input-reflectionless QET wideband BPF prototype shown in Fig. 9. (a) Theoretical, EM-simulated, circuit model, and measured power transmission ($|S_{21}|$) and input reflection ($|S_{11}|$) responses. (b) Theoretical, simulated, and measured power absorption ratios [i.e., $100\times(1-|S_{21}|^2-|S_{11}|^2)$ (%)]. (c) Simulated and measured in-band group delay (τ_g) responses. (d) Photograph (top/bottom view) of the assembled BPF prototype.

Fig. 11. Conceptual block diagram of the proposed input-reflectionless high-order QET wideband BPF based on the in-series cascade connection of multiple replicas of the input-reflectionless BPF unit with $i = 0$ and $M = 1$.

BPF prototype. A fairly close agreement among the theoretical, EM-simulated, circuit model, and measured results is obtained in Fig. 10(a). As proven, an input-reflectionless QET wideband filtering response with further enhanced passband amplitude flatness is attained. As a minor discrepancy between measurements and predictions, note that the in-band power insertion loss profile at the upper frequency band edge region is slightly degraded. This is mainly attributed to the dispersion and radiation effects of the slotline resonator exploited in the design of such multilayered wideband BPFs [37]. The main performance metrics of the measured BPF are as follows: center frequency of 1.989 GHz, minimum in-band power insertion loss level of 0.48 dB, 3-dB FBW of 78.5%, 1-dB FBW of 66.04%, and stopband power attenuation and input power-matching levels above 16.12 and 13.98 dB, respectively. The passband flatness factor for this circuit, which is calculated as 84.13%, is superior to the one of the first prototype in Fig. 7, hence confirming the expectations. Moreover, compared with the measured power absorption ratios in Fig. 7(b), the measured data in Fig. 10(b) reveal a response with an increased minimum stopband power absorption ratio level above 96.02% from 0 to 4.9 GHz (i.e., without considering the passband range) and a minimum in-band power absorption ratio of 8.81% measured at 1.91 GHz. The measured maximum in-band group delay variation is 0.38 ns [see Fig. 10(c)].

C. Higher Order Input-Reflectionless Wideband BPF

Although the BPF prototype reported in Section II-B features a QET wideband filtering response with enhanced passband amplitude flatness and improved stopband power absorption ratio levels, it still suffers from relatively poor out-of-band power attenuation levels. To overcome this issue, higher order wideband BPF schemes with increased stopband power attenuation levels can be devised by means of the in-series cascade of n replicas of the engineered wideband BPF shown in Fig. 6, which acts as broadband input-absorptive BPF unit. The conceptual block diagram of this type of higher order wideband BPF is shown in Fig. 11. Based on the exploited impedance values of the wideband BPF unit, examples of the theoretical power transmission and input reflection responses of this proposed high-order wideband BPF with one, two, and three stages are compared in Fig. 12. As shown, the stopband power attenuation levels of the devised high-order wideband BPF are highly improved by the number of cascaded BPF stages and the selectivity of the associated power transmission coefficients is increased accordingly, whereas their input power reflection levels at the stopband regions remain almost unaltered.

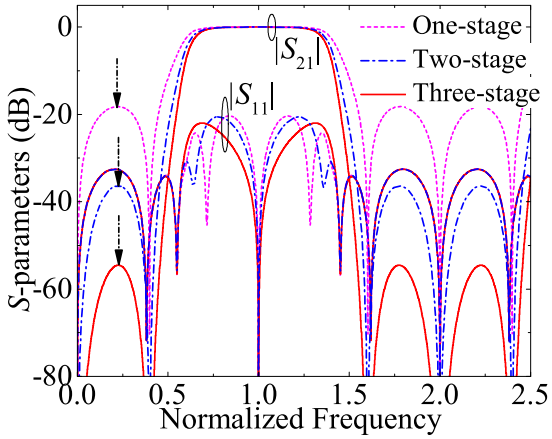

Fig. 12. Theoretical power transmission ($|S_{21}|$) and input reflection ($|S_{11}|$) responses of the proposed input-reflectionless high-order QET wideband BPF ($Z_0 = 50\ \Omega$) in Fig. 11 with one, two, and three replicas, respectively, of the wideband BPF unit in Section II-A with $i = 0$ and $M = 1$ when $Z_m = 45.0114\ \Omega$, $Z_s = 57.7969\ \Omega$, $Z_1 = 39.6298\ \Omega$, $Z_2 = 76.0365\ \Omega$, $Z_{m1} = 90.6474\ \Omega$, $Z_{m2} = 67.3283\ \Omega$, $Z_{m3} = 56.4916\ \Omega$, and $R = 50\ \Omega$.

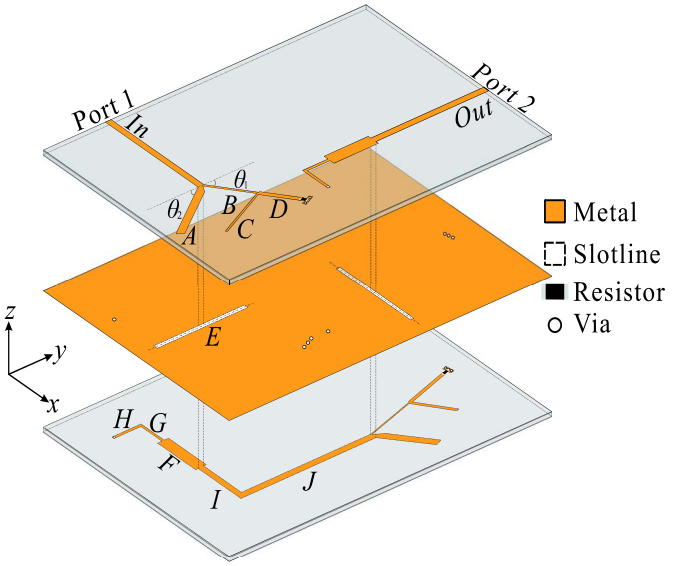

Fig. 13. 3-D layout of the developed input-reflectionless high-order QET wideband BPF prototype using two in-series cascaded wideband BPF units with shunt resistively terminated microstrip T-junctions ($L_{\rm In} = L_{\rm Out} = 52$, $L_{\rm A} = 21.25$, $L_{\rm B} = 23.45$, $L_{\rm C} = 22.87$, $L_{\rm D} = 22.65$, $L_{\rm E} = 49.46$, $L_{\rm F} = 21.59$, $L_{\rm G} = 12$, $L_{\rm H} = 11.3$, $L_{\rm I} = 30$, $L_{\rm J} = 50$, $W_{\rm In} = W_{\rm Out} = W_{\rm I} = W_{\rm J} = 1.82$, $W_{\rm A} = 2.42$, $W_{\rm B} = 0.54$, $W_{\rm C} = 1.3$, $W_{\rm D} = 1.6$, $W_{\rm E} = 0.24$, $W_{\rm F} = 2.86$, $W_{\rm G} = W_{\rm H} = 0.96$ (unit: mm), $\theta_1 = 75°$, and $\theta_2 = 30°$).

To verify the experimental viability of this suggested higher order wideband BPF principle, a circuit prototype using two cascaded third-order input-reflectionless wideband BPFs shown in Fig. 6 is simulated and characterized. The 3-D circuit layout of the conceived two-wideband BPF unit prototype is provided in Fig. 13. Here, a nearly full-wavelength 50-Ω microstrip line section printed on the bottom layer is arranged in a folded structure and used to connect two third-order wideband BPF units during the EM simulation. The measured resistance values of the two used SMD resistors are 50.1 and 50.5 Ω, respectively. The theoretical, EM-simulated, circuit model, and measured power transmission and input reflection responses of this developed

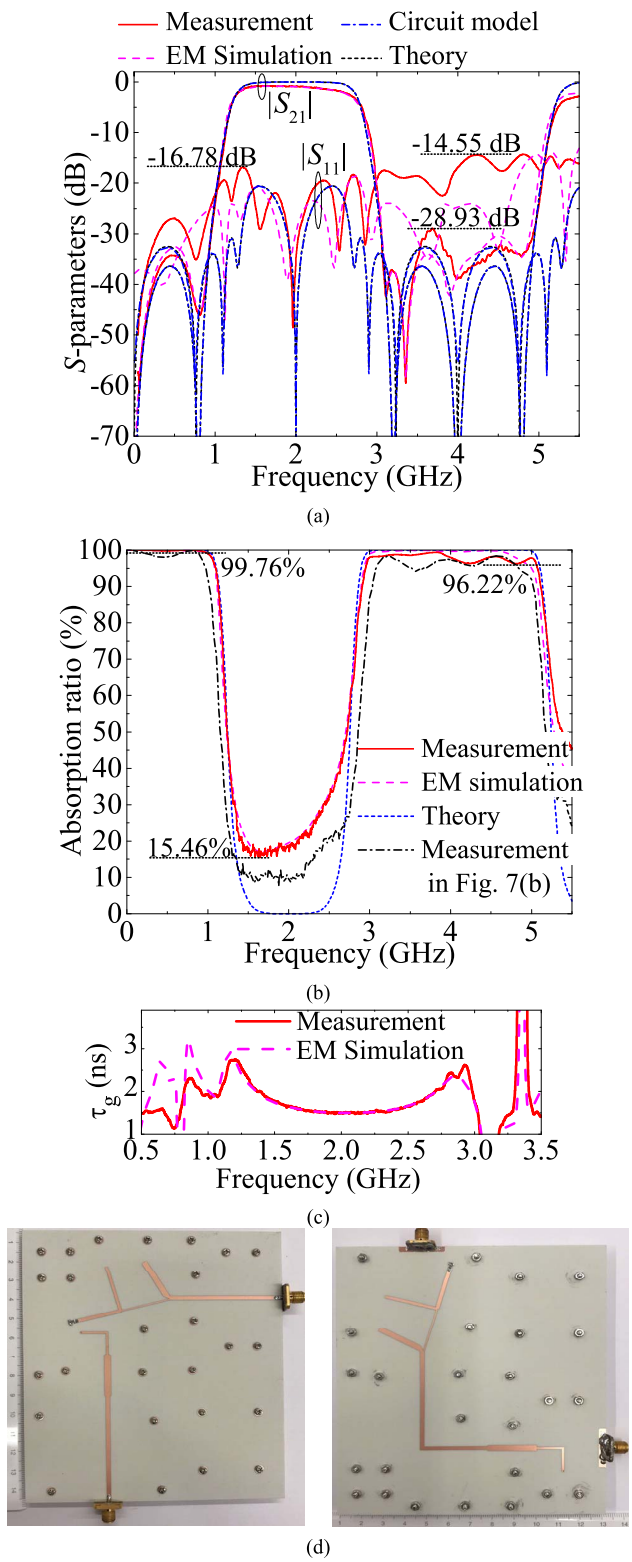

Fig. 14. Frequency responses of the manufactured input-reflectionless high-order QET wideband BPF prototype shown in Fig. 13. (a) Theoretical, EM-simulated, circuit model, and measured power transmission ($|S_{21}|$) and input reflection ($|S_{11}|$) responses. (b) Theoretical, simulated, and measured power absorption ratios [i.e., $100\times(1 - |S_{21}|^2 - |S_{11}|^2)$ (%)]. (c) Simulated and measured in-band group delay (τ_g) responses. (d) Photograph (top/bottom view) of the assembled BPF prototype.

wideband BPF prototype are plotted in Fig. 14(a). As shown, the expected higher power attenuation levels of these curves

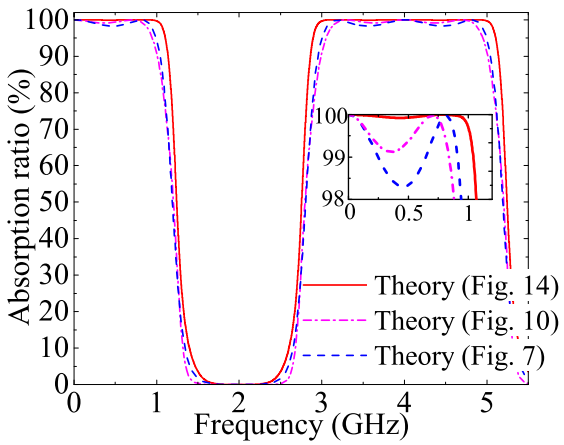

Fig. 15. Comparison of the theoretical power absorption ratio profiles of the three proposed input-reflectionless QET wideband BPFs with their circuit layouts depicted in Figs. 6, 9, and 13, respectively.

are obtained, and a fairly close agreement among them is attained. Similarly, due to the frequency dispersion and radiation effects attributed to the slotline resonators, the simulated and measured in-band power insertion loss levels of this designed wideband BPF increase gradually at the passband high-frequency region. The measured wideband BPF is centered at 1.987 GHz with a minimum in-band power insertion loss level of 0.75 dB, 1-dB FBW of 60.9%, and 3-dB FBW of 77.3%—i.e., passband flatness factor of 78.78%. A minimum stopband power attenuation level of 28.93 dB and input power-matching levels above 14.54 dB from 0 to 5.5 GHz are measured. Besides, a minimum stopband power absorption ratio level above 96.22% from 0 to 5.06 GHz (i.e., without considering the passband range) and a minimum in-band power absorption ratio of 15.46% at 1.79 GHz are measured, as shown in Fig. 14(b). Compared with the measured data in Fig. 7(b), a remarkably improved sharpness of the power absorption ratio profile within the stopband-to-passband transitions is demonstrated, which is mainly attributed to the exploited higher order BPF topology. The maximum in-band group delay variation is measured to be 1.38 ns in Fig. 14(c). The top- and bottom-view photographs of the assembled high-order wideband BPF prototype are shown in Fig. 14(d).

To conclude this section, a comparison in terms of theoretical power absorption ratio curves for the three designed input-reflectionless QET wideband BPFs (i.e., circuit layouts in Figs. 6, 9, and 13) is provided in Fig. 15. As shown, using the resistively terminated higher order LPF network, increased stopband power absorption ratio levels and enhanced in-band amplitude flatness for the whole BPF are attained. On the other hand, for the high-order wideband BPF based on two in-series-cascaded input-absorptive BPF units, almost perfect stopband power absorption ratio levels and highly improved sharpness in its power absorption ratio profile within the stopband-to-passband transitions are attained. However, this is achieved at the expense of some in-band flatness deterioration owing to its two used resistively ended BSF branches (one per BPF unit).

III. Fourth-Order Wideband Balun BPF With a Shunt Resistively Terminated Microstrip T-Junction

As multiport filtering device example, the applicability of the previous shunt resistively terminated microstrip T-junction to design an input-reflectionless fourth-order wideband balun BPF with QET filtering response is addressed here. Compared with the input-absorptive wideband balun reported in [27] with relatively poor performance, the broadband balun BPF in this work is synthetically designed with a detailed design procedure and expected to be realized with merits in terms of higher filtering selectivity, enhanced passband amplitude flatness, and improved stopband power absorption ratios. The diplexer-based equivalent circuit of the proposed three-port balun is depicted in Fig. 16(a). Instead of the reflective-type fourth-order wideband balun BPF using paired short-circuit-ended quarter-wavelength stubs in [40], the engineered input-reflectionless balun is modified with a pair of shunt-connected open-circuit-ended half-wavelength stubs loaded at the two output ports and a shunt resistively terminated TL T-junction connected at the input port. Except for the paired open-circuit-ended stubs at the output ports that are designed with characteristic impedance Z_3 and electrical length $2\theta = \pi$ (i.e., half-wavelength-long at f_0), the electrical lengths of the open-circuit-ended stub, the short-circuit-ended stubs, the two in-series TL sections of the balun channel, as well as the cascaded TL sections and the open-circuit-ended stub of the lossy BSF channel (i.e., absorptive LPF T-junction) are set as $\theta = \pi/2$ (i.e., quarter-wavelength-long at f_0). However, they exhibit different characteristic impedances Z_m, Z_s, Z_1, Z_2, Z_{m1}, Z_{m2}, and Z_{m3}. Similarly, four transformers with different turns ratios N_m, N_s, N_{m1}, and N_{m2} are used to feature the impedance variations in the coupled microstrip lines/sections and the slotline resonator in the EM simulation process.

To analyze the RF operational principles of this three-port balun BPF, its two-port equivalent circuit that serves as wideband 50-to-100-Ω ($Z_0 = 50\ \Omega$) impedance transformer is derived, as shown in Fig. 16(b). Here, the equivalent impedances of the cascaded TL sections and open-circuit-ended stubs of the reflective-type balun channel are represented as $2Z_1$, $2Z_2$, and $2Z_3$. Moreover, Z_{in}, $Z_{\text{in}a}$, and $Z_{\text{in}b}$ refer to the input impedances of the corresponding building blocks of this input-reflectionless broadband impedance transformer.

With the obtained *ABCD* matrix for the reflective-type-balun BPF channel of this two-port impedance transformer network in Fig. 16(b), its wideband frequency response is first discussed with $N_m = N_s = N_{m1} = N_{m2} = 1$. By assuming $Z_{01} = Z_0$ and $Z_{02} = 2Z_0$ as the source and load port impedances, its power transmission (S_{21}) and reflection (S_{11}) coefficients [41] as well as its characteristic function F_{M3} are formulated as follows:

$$S_{21} = \frac{2\sqrt{z_{01}z_{02}}}{A_3 z_{02} + B_3 + C_3 z_{01} z_{02} + D_3 z_{01}} \tag{21}$$

$$S_{11} = \frac{A_3 z_{02} + B_3 - C_3 z_{01} z_{02} - D_3 z_{01}}{A_3 z_{02} + B_3 + C_3 z_{01} z_{02} + D_3 z_{01}} \tag{22}$$

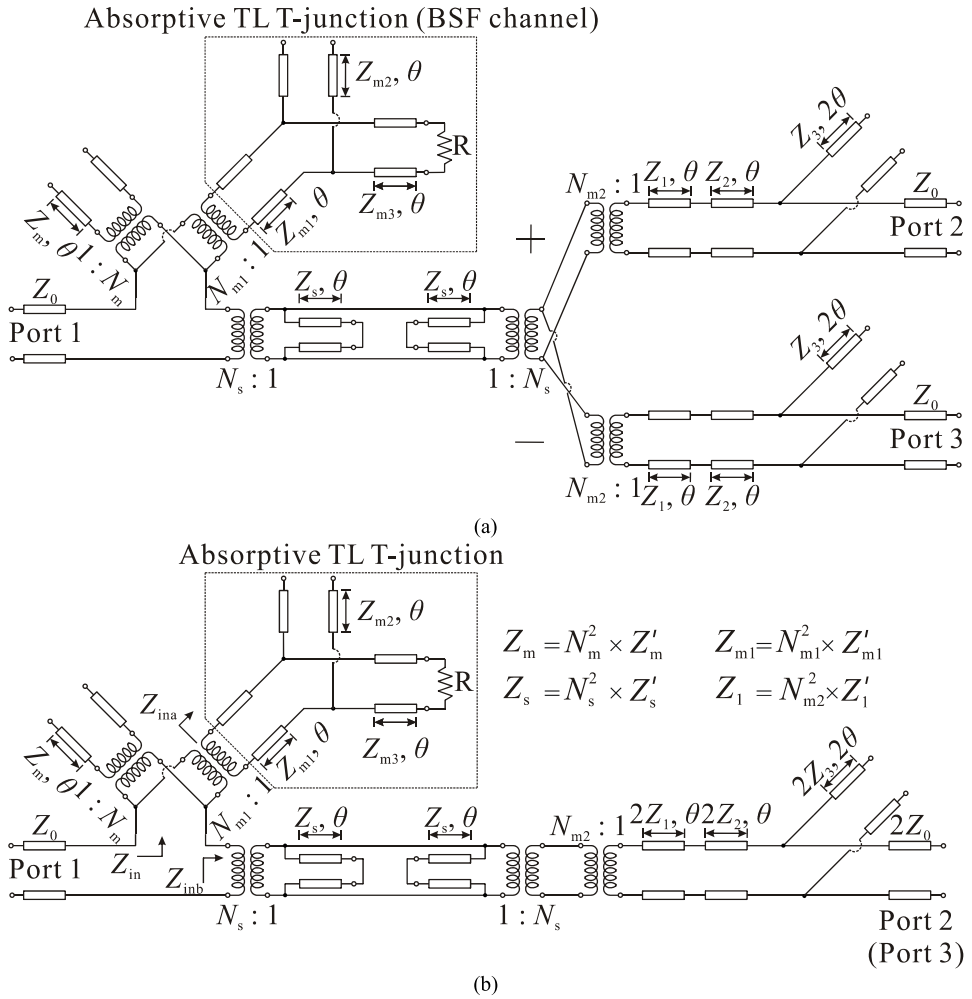

Fig. 16. Diplexer-based TL equivalent circuit of the proposed input-reflectionless QET fourth-order wideband balun BPF. (a) Three-port equivalent circuit by means of a modified fourth-order vertical-transition-based balun BPF and a shunt resistively terminated TL T-junction. (b) Simplified two-port equivalent circuit exploited as input-reflectionless wideband 50-to-100-Ω ($Z_0 = 50\ \Omega$) impedance transformer.

$$F_{M3} = \frac{(A_3 z_{02} - D_3 z_{01}) + (B_3 - C_3 z_{01} z_{02})}{2\sqrt{z_{01} z_{02}}} \tag{23}$$

where

$$A_3 = -\frac{2z_m}{z_s}\frac{\cos^4\theta}{\sin^2\theta} + \left(1 + \frac{z_m}{2z_1} + \frac{z_1}{z_2} + \frac{2z_m z_1}{z_s z_2} + \frac{z_m}{2z_2}\right)\cos^2\theta - \frac{z_1}{z_2} - \left(\frac{2z_2}{z_3} + \frac{2z_1}{z_3} + \frac{z_m z_2}{z_1 z_3}\right)\frac{\cos^2\theta}{1 - 2\sin^2\theta} + \left(\frac{2z_2}{z_3} + \frac{2z_1}{z_3} + \frac{z_m z_2}{z_1 z_3} + \frac{z_m}{z_3} + \frac{4z_m(z_1 + z_2)}{z_s z_3}\right) \times \frac{\cos^4\theta}{1 - 2\sin^2\theta} \tag{24a}$$

$$B_3 = j\left(2z_1 + 2z_2 + \frac{z_m z_2}{z_1}\right)\sin\theta\cos\theta - j \times \left(z_m + \frac{4z_m z_1}{z_s} + \frac{4z_m z_2}{z_s}\right)\frac{\cos^3\theta}{\sin\theta} \tag{24b}$$

$$C_3 = j\left(\frac{1}{2z_1} + \frac{1}{2z_2} + \frac{2z_1}{z_s z_2}\right)\sin\theta\cos\theta - j\frac{2}{z_s}\frac{\cos^3\theta}{\sin\theta} - j\frac{z_2}{z_1 z_3}\frac{\sin\theta\cos\theta}{1 - 2\sin^2\theta} + j\left(\frac{1}{z_3} + \frac{z_2}{z_1 z_3} + \frac{4z_1}{z_s z_3} + \frac{4z_2}{z_s z_3}\right) \times \frac{\sin\theta\cos^3\theta}{1 - 2\sin^2\theta} \tag{24c}$$

$$D_3 = \left(\frac{z_2}{z_1} + \frac{4z_1 + 4z_2}{z_s} + 1\right)\cos^2\theta - \frac{z_2}{z_1} \tag{24d}$$

and z_m, z_s, z_1, z_2, and z_3 are the normalized impedances, while z_{01} and z_{02} are the normalized port impedances. In addition to the inherent power TZs at 0 and $2f_0$ for which $|S_{21}| = 0$, two additional real-frequency TZs generated by the open-circuit-ended half-wavelength stub are created at $f_0/2$ and $3f_0/2$. Here, this balun BPF channel is also desired to be designed with a reflective-type QET Chebyshev equal-ripple response. By following the design approach provided in Section II-A, the frequency response of this balun BPF channel as well as the ones related to the real and imaginary parts of its F_{M3} function is calculated. Unlike the assumptions for the QET three-pole reflective-type BPF in Fig. 3, the proposed balun BPF features the expected QET fourth-order reflective-type Chebyshev in-band equal-ripple profile for the real part (i.e., $A_3 z_{02} - D_3 z_{01}$) of F_{M3}. With the predefined design specifications of the Chebyshev equal-ripple response [40], the impedances of the balun BPF channel are

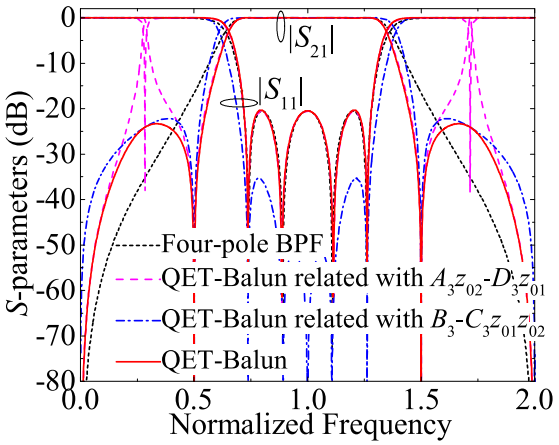

Fig. 17. Theoretical power transmission ($|S_{21}|$) and reflection ($|S_{11}|$) responses of the proposed two-port 50-to-100-Ω fourth-order reflective-type wideband QET impedance transformer BPF channel without considering the absorptive TL T-junction when $z_m = 1.9505$, $z_s = 0.7851$, $z_1 = 1.0866$, $z_2 = 1.3976$, and $z_3 = 1.4613$.

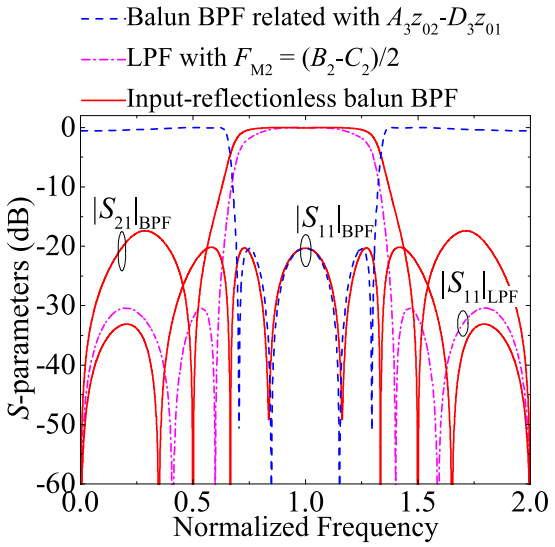

Fig. 18. Theoretical power transmission ($|S_{21}|$) and reflection ($|S_{11}|$) responses of the proposed two-port 50-to-100-Ω input-reflectionless fourth-order QET wideband impedance transformer with $z_m = 1.267$, $z_s = 0.8466$, $z_1 = 1.086$, $z_2 = 1.394$, $z_3 = 1.572$, $z_{m1} = 1.5798$, $z_{m2} = 1.5462$, and $z_{m3} = 1.144$, its relevant reflective-type fourth-order $|S_{11}|$ associated with the real part of F_{M3} to meet the specified Chebyshev in-band equal-ripple responses with $z_m = 1.271$, $z_s = 0.9066$, $z_1 = 1.086$, $z_2 = 1.394$, $z_3 = 1.572$, $z_{m1} = 1.5798$, $z_{m2} = 1.5462$, and $z_{m3} = 1.144$, and the reflective-type $|S_{11}|$ of the reshaped input-reflectionless fifth-order LPF network resulting from $F_{M2} = (B_2 - C_2)/2$ to satisfy the specified Chebyshev equal-ripple LPF response with $z_m = 1.267$, $z_s = 0.8466$, $z_1 = 1.086$, $z_2 = 1.394$, $z_3 = 1.572$, $z_{m1} = 1.6432$, $z_{m2} = 1.5462$, and $z_{m3} = 1.144$.

quantitatively determined. As a design example, by choosing $L_{A3} = 0.039$ or RL = 20.49 dB, $\theta_{c3} = 64.71°$, and $n = q = 2$ as described in [40], a fourth-order Chebyshev equal-ripple response with its transmission poles at $0.7397f_0$, $0.8908f_0$, $1.1091f_0$, and $1.2603f_0$ is obtained. Then, by means of these predefined transmission poles and (21)–(24), the impedances (i.e., z_m, z_s, z_1, z_2, and z_3) of the proposed QET balun BPF channel are determined to fulfill the specified Chebyshev in-band equal-ripple responses, which yields $z_m = 1.9505$, $z_s = 0.7851$, $z_1 = 1.0866$, $z_2 = 1.3976$, and $z_3 = 1.4613$. As illustrated in Fig. 17, the desired fourth-order QET reflective-type Chebyshev equal-ripple response for the proposed balun BPF is then obtained, and the power reflection coefficient associated with the real part of F_{M3} features the specified Chebyshev in-band equal-ripple response. Although two spurious transmission peaks appear at the lower and higher stopband regions for the real part of F_{M3}, they are counteracted in the overall response by the effect of the F_{M3} imaginary part.

Next, the input-reflectionless property of the proposed two-port wideband impedance transformer with a shunt resistively terminated TL T-junction is analyzed. With $z_{ina} = ja/(b^2 + c^2)$ and z_{in} in (10)–(12), the *ABCD* elements of this diplexer-based input-reflectionless impedance transformer are calculated. To exactly determine its constituent z_m, z_s, z_1, z_2, z_3, z_{m1}, z_{m2}, and z_{m3}, the in-band reflective-type frequency response associated with the real part of F_{M3} of this QET impedance transformer must be forced to be equal to the referred fourth-order Chebyshev equal-ripple response with the specified L_{A3} and θ_{c3} [40]. On the other hand, as discussed in Section II-A, the reshaped BSF channel, which is built by ending the output port (Port 2 or Port 3) of the proposed impedance transformer with a 100-Ω port impedance and by replacing the resistor R with an output port, actually features an input-absorptive fifth-order LPF behavior. Herein, the normalized impedance z_{inb} is reformulated as

$$z_{inb} = \frac{(a_2c_2 + b_2d_2) + j(b_2c_2 - a_2d_2)}{c_2^2 + d_2^2} \tag{25}$$

where

$$\begin{aligned} a_2 &= -\left(16z_1^2z_2z_s + 16z_1z_2^2z_s\right)\tan^3\theta \\ &\quad + \left(8z_1z_2z_3z_s - 8z_1^2z_3z_s\tan^2\theta\right)(1 - \tan^2\theta)\tan\theta \qquad (26a) \\ b_2 &= \left(8z_1z_2^2z_3z_s + 8z_1^2z_2z_3z_s\right)(1 - \tan^2\theta)\tan^2\theta \qquad (26b) \\ c_2 &= \left(16z_1^2z_2z_3 + 16z_1z_2^2z_3 + 4z_1z_2z_3z_s - 4z_2^2z_3z_s\tan^2\theta\right) \\ &\quad \times (1 - \tan^2\theta)\tan\theta \qquad (26c) \\ d_2 &= \left(32z_1^2z_2 + 32z_1z_2^2 + 8z_1z_2z_s\right)\tan^2\theta - 8z_2^2z_s\tan^4\theta \\ &\quad - 16z_1z_2z_3(1 - \tan^2\theta) + \left(16z_1^2z_3 + 4z_1z_3z_s + 4z_2z_3z_s\right) \\ &\quad \times (1 - \tan^2\theta)\tan^2\theta. \qquad (26d) \end{aligned}$$

With (14a)–(14d), (25), and (26), the frequency response of this reshaped lossy LPF network is determined. In particular, its fifth-order reflective-type Chebyshev in-band equal-ripple LPF response, which is related to $F_{M2} = (B_2 - C_2)/2$ and $z_{inb} = j(b_2c_2 - a_2d_2)/(c_2^2 + d_2^2)$ with the utilized z_m, z_s, z_1, z_2, z_3, z_{m1}, z_{m2}, and z_{m3}, is expected to meet the theoretical one associated with the Chebyshev LPF polynomial for the specified L_{A2}, θ_{c2}, and (17)–(20). In this context, a fourth-order reflective-type Chebyshev in-band equal-ripple BPF response with $L_{A3} = 0.04071$ dB or RL = 20.3 dB and $\theta_{c3} = 62.37°$ in the proposed whole impedance transformer for the real part of F_{M3} and $z_{ina} = ja/(b^2 + c^2)$ is realized. Such response must meet the specified reflective-type Chebyshev equal-ripple LPF response with $L_{A2} = 0.00421$ dB and $\theta_{c2} = 55.62°$ for the reshaped input-reflectionless fifth-order LPF with $F_{M2} = (B_2 - C_2)/2$ and $z_{inb} = j(b_2c_2 - a_2d_2)/(c_2^2 + d_2^2)$, for which the values of z_m, z_s, z_1, z_2, z_3, z_{m1}, z_{m2},

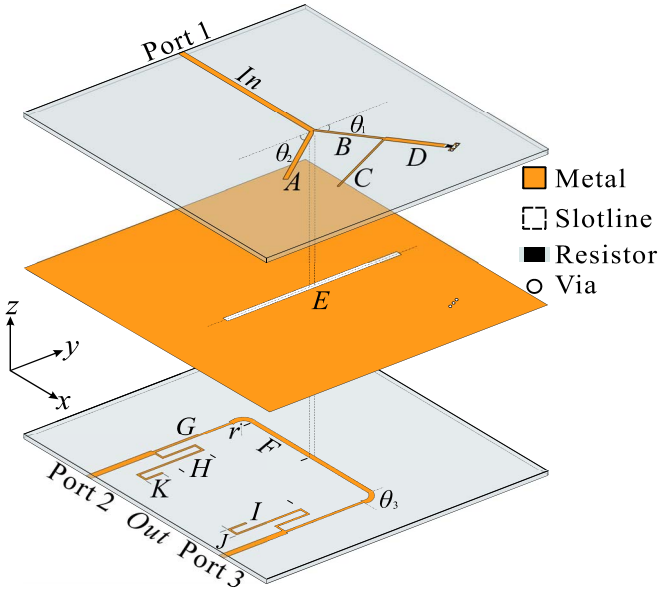

Fig. 19. 3-D layout of the devised input-reflectionless fourth-order wideband QET balun BPF prototype using a shunt resistively terminated microstrip T-junction ($L_{\rm In} = 45$, $L_{\rm Out} = 29.4$, $L_{\rm A} = 28.68$, $L_{\rm B} = 29.17$, $L_{\rm C} = 29.1$, $L_{\rm D} = 28.05$, $L_{\rm E} = 60.8$, $L_{\rm F} = 26.19$, $L_{\rm G} = 29.11$, $L_{\rm H} = 13.97$, $L_{\rm I} = 32$, $L_{\rm J} = 3$, $L_{\rm K} = 6.33$, $r = 1$, $W_{\rm In} = W_{\rm Out} = 0.54$, $W_{\rm A} = 0.26$, $W_{\rm B} = 0.2$, $W_{\rm C} = 0.13$, $W_{\rm D} = 0.44$, $W_{\rm E} = 0.15$, $W_{\rm F} = 0.44$, $W_{\rm G} = 0.18$, $W_{\rm H} = W_{\rm I} = W_{\rm J} = W_{\rm K} = 0.12$ (unit: mm), and $\theta_1 = 75°$, $\theta_2 = 30°$, and $\theta_3 = 90°$).

and z_{m3} are quantitatively determined. Fig. 18 represents the power transmission and reflection responses of the mentioned fourth-order reflective-type Chebyshev in-band equal-ripple BPF and the fifth-order reflective-type Chebyshev equal-ripple LPF that are attained for two sets of the design impedances, for which only the values of z_m, z_s, and z_{m1} are different. To forcedly make the proposed input-reflectionless QET wideband impedance transformer feature the desired fourth-order Chebyshev in-band equal-ripple response, the value of z_{m1} of the determined second set of impedances is slightly adjusted so that $z_m = 1.267$, $z_s = 0.8466$, $z_1 = 1.086$, $z_2 = 1.394$, $z_3 = 1.572$, $z_{m1} = 1.5798$, $z_{m2} = 1.5462$, and $z_{m3} = 1.144$.

To practically demonstrate the viability of this proposed input-reflectionless wideband QET balun BPF, a proof-of-concept microstrip circuit is designed, manufactured, and tested. The 3-D layout of the developed diplexer-based wideband balun BPF implemented in a two-layered structure is illustrated in Fig. 19. Here, the open-circuit-ended stub, the short-circuit-ended stubs, the in-series TL sections, the open-circuit-ended stubs at the output ports, and the resistively terminated TL T-junction depicted in Fig. 16 are realized as an open-circuit-ended microstrip resonator on the top layer, a slotline resonator, back-to-back cascaded microstrip sections, open-circuit-ended microstrip lines shaped in a meandered line structure on the bottom layer, and a shunt microstrip T-junction, respectively. Meanwhile, the RT/Duroid 6010 substrate with relative dielectric constant $\varepsilon_{\rm r} = 10.8$, dielectric thickness $h = 0.635$, metal thickness $t = 35$ μm, and dielectric loss tangent $\tan(\delta_{\rm D}) = 0.0027$ is used. An SMD resistor with a measured resistance of 49.9 Ω is soldered in the output port of the absorptive BSF channel. As discussed,

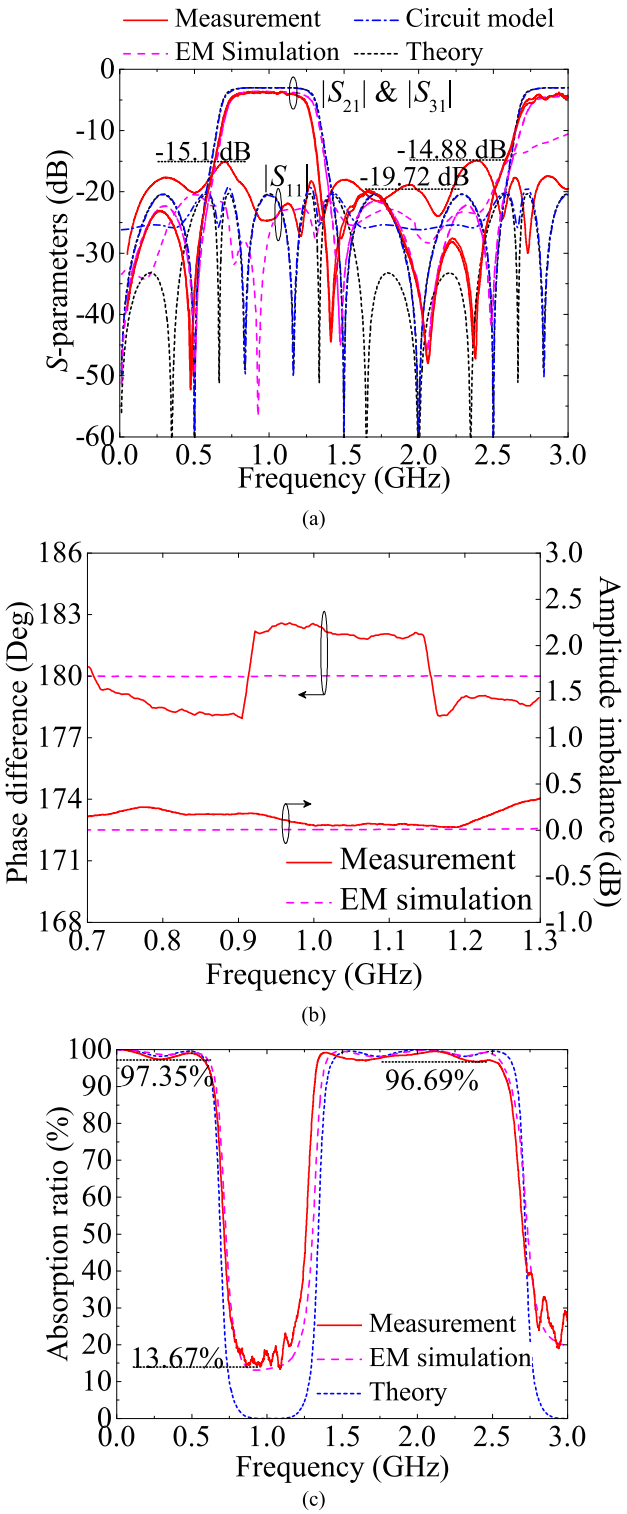

Fig. 20. Frequency responses of the manufactured input-reflectionless fourth-order wideband balun BPF prototype shown in Fig. 19. (a) Theoretical, EM-simulated, circuit model, and measured power transmission ($|S_{21}|$ and $|S_{31}|$) and input reflection ($|S_{11}|$) responses. (b) Simulated and measured amplitude imbalance and phase difference. (c) Theoretical, simulated, and measured power absorption ratios [i.e., $100\times(1 - |S_{21}|^2 - |S_{31}|^2 - |S_{11}|^2)$ (%)].

this proposed input-reflectionless fourth-order wideband balun BPF centered at $f_0 = 1$ GHz is initially designed with $Z_m = 63.35$ Ω, $Z_s = 42.33$ Ω, $Z_1 = 54.3$ Ω, $Z_2 = 69.7$ Ω,

TABLE I
COMPARISON WITH OTHER PRIOR ART REFLECTIONLESS WIDEBAND BPFS AND BALUN BPFS

Ref.	3-dB FBW /f_0 (GHz)	In-band IL/RL (dB)	Stopband PAL	Stopband PARs	RR (GHz) /RL (dB)	Flatness factor	Reflectionless behavior	QET response
[26] BPF in Fig. 6	90.1%/1.91	≤ 0.49/≥ 19.27	N/A	N/A	0.01–4.5/≥13.17	45.8%	Two-port	No
[26] BPF in Fig. 10	80.3%/2.04	≤ 0.48/≥ 20.88	N/A	N/A	0.01–4.5/≥17.33	68.7%	Two-port	No
[26] BPF in Fig. 14	89.5%/2.03	≤ 0.52/≥ 23.58	N/A	N/A	0.01–4.5/≥11.17	64.3%	Two-port	No
[26] BPF in Fig. 17	81.1%/2.05	≤ 0.36/≥ 20.55	N/A	N/A	0.01–4.5/≥13.81	84.5%	Two-port	No
[26] BPF in Fig. 21	81.5%/2	≤ 0.9/≥ 21.62	N/A	N/A	0.01–4.5/≥11.06	49.2%	Two-port	No
[27] Balun in Fig. 5	98.8%/1.99	≤ 3.58/≥ 14.62	N/A	N/A	0.01–5/≥10.98	73.44%	Input	No
BPF in Fig. 7	86.78%/2.004	≤ 0.37/≥ 15.58	≥ 13.7	≥ 94.1%	0.01–5.5/≥ 13.52	81.91%	Input	Yes
BPF in Fig. 9	78.5%/1.989	≤ 0.48/≥ 18.92	≥ 16.12	≥ 96.02%	0.01–5.5/≥ 13.98	84.13%	Input	Yes
BPF in Fig. 13	77.3%/1.987	≤ 0.75/≥ 16.78	≥ 28.93	≥ 96.22%	0.01–5.5/≥ 14.55	78.78%	Input	Yes
Balun in Fig. 17	56.78%/0.988	≤ 3.67/≥ 15.1	≥ 19.72	≥ 96.69%	0.01–3/≥ 14.88	84.5%	Input	Yes

Flatness factor: ratio between the 1-dB and 3-dB FBWs; PAL: power-attenuation level; PARs: power-absorption ratios; RR: Reflectionless range.

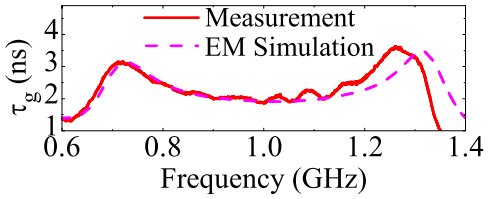

Fig. 21. Simulated and measured in-band group delay (τ_g) responses of the proposed input-reflectionless fourth-order wideband balun BPF.

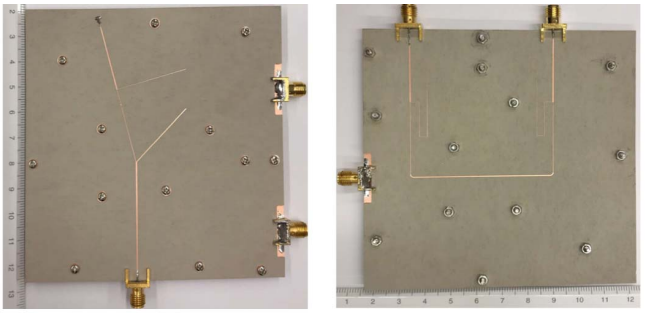

(a) (b)

Fig. 22. Photographs of the assembled input-reflectionless fourth-order wideband balun BPF. (a) Top view. (b) Bottom view.

$Z_3 = 78.6\ \Omega$, $Z_{m1} = 78.99\ \Omega$, $Z_{m2} = 77.31\ \Omega$, $Z_{m3} = 57.2\ \Omega$, and $R = 50\ \Omega$. However, to make the EM-simulated responses reasonably close to the theoretical ones, $Z'_{\rm m} = 65.89\ \Omega$, $Z'_{\rm s} = 58.59\ \Omega$, $Z'_1 = 54.19\ \Omega$, $Z_2 = 69.7\ \Omega$, $Z_3 = 78.6\ \Omega$, $Z'_{\rm m1} = 71.61\ \Omega$, $Z_{m2} = 77.3\ \Omega$, and $Z_{m3} = 57.2\ \Omega$ are chosen. Hence, the turns ratios of the used transformers with $N_m = 0.979$, $N_s = 0.85$, $N_{m1} = 1.05$, and $N_{m2} = 1.001$ are extracted.

The comparison among the theoretical, EM-simulated, circuit model, and measured power transmission and input-reflection responses of the devised wideband balun BPF prototype is provided in Fig. 20(a). As shown, four-pole input-reflectionless wideband responses with high selectivity and enhanced passband amplitude flatness are simulated and measured. In the measurement, relatively increased insertion loss levels and a narrower FBW are obtained, which is mostly attributed to the dispersion effect on the characteristic impedance of the slotline resonator with low impedance value and to manufacturing tolerances. The measured performance metrics of this engineered wideband balun BPF prototype are as follows: center frequency of 0.988 GHz with minimum in-band power insertion loss of 3.67 dB (0.67-dB excess loss with regard to the 3-dB division factor inherent to the balun circuit action), 1-dB FBW from 0.745 GHz to 1.219 GHz (i.e., of 47.98 %), and 3-dB FBW from 0.707 GHz to 1.268 GHz (i.e., of 56.78%)—leading to a passband flatness factor of 84.5, minimum out-of-band power attenuation level of 19.72 dB, and input power-matching levels above 14.88 dB within the represented spectral range from 0 to 3 GHz. The measured in-band amplitude and phase imbalances are below 0.35 dB and 2.61°, respectively, as shown in Fig. 20(b). Moreover, as observed in Fig. 20(c), a minimum stopband power absorption ratio of 96.69% from 0 to 2.52 GHz (i.e., without considering the passband range) and a minimum in-band power absorption ratio of 13.67% at 0.954 GHz are measured. The maximum in-band group delay variation, as derived from the results in Fig. 21, is measured as 1.78 ns. In addition, Fig. 22 presents the top- and bottom-view photographs of the assembled fourth-order wideband balun BPF prototype.

IV. COMPARISON WITH THE STATE-OF-THE-ART

A detailed comparison between the input-reflectionless QET wideband filtering circuits developed in this study and other prior art reflectionless wideband BPFs and baluns is provided in Table I. As can be seen, the engineered wideband BPF and balun BPF prototypes exhibit the expected merits in terms of high filtering selectivity, enhanced passband amplitude

flatness, and improved stopband power absorption ratios with increased sharpness in their frequency profiles within the stopband-to-passband transitions. It must be fairly recognized that the measured in-band power-matching levels for the developed wideband BPF and balun BPF prototypes of this work are below the prescribed 20-dB value achieved during the EM simulation process. This is mainly attributed to the manufacturing tolerances and the unremoved port discontinuity effect in the assembled circuits for their testing.

V. Conclusion

The development of a class of two-layered diplexer-based input-reflectionless wideband QET filtering devices has been presented. First, a third-order wideband BPF exploiting a modified wideband microstrip vertical transition and a shunt resistively terminated microstrip T-junction has been reported. Its RF operational principles and its design procedure to theoretically determine the impedance-type design parameters have been detailed with the provided synthesis method. Then, to validate the effectiveness of the absorptive high-order LPF network to further enhance passband amplitude flatness and stopband power absorption ratio profile, an alternative third-order wideband BPF using a shunt resistively terminated microstrip π-shape structure has been proposed. Subsequently, to highly increase the stopband power attenuation levels, a high-order wideband BPF based on the in-series cascade of two third-order wideband BPF units using the absorptive microstrip T-junctions has been engineered. Additionally, to verify the applicability of the devised filter approaches on designing multiport components, a fourth-order input-reflectionless QET wideband balun BPF using a shunt resistively terminated microstrip T-junction has been conceived. Four demonstrative prototypes of these wideband BPF and balun BPF topologies have been manufactured and measured. They have featured the expected merits in terms of broadband QET filtering responses, enhanced passband amplitude flatness, and improved stopband power absorption ratios, thus validating the suggested absorptive/reflectionless broadband filter design techniques.

References

[1] B. Mini-Circuits, "Reflectionless filters improve linearity and dynamic range," *Microw. J.*, vol. 58, no. 8, pp. 42–50, Aug. 2015.

[2] M. A. Morgan, "Think outside the band: Design and miniaturization of absorptive filters," *IEEE Microw. Mag.*, vol. 19, no. 7, pp. 54–62, Nov. 2018.

[3] R. Gomez-Garcia, D. Psychogiou, J.-M. Munoz-Ferreras, and L. Yang, "Avoiding RF isolators: Reflectionless microwave bandpass filtering components for advanced RF front ends," *IEEE Microw. Mag.*, vol. 21, no. 12, pp. 68–86, Dec. 2020.

[4] A. C. Guyette, I. C. Hunter, and R. D. Pollard, "Design of absorptive microwave filters using allpass networks in a parallel-cascade configuration," in *IEEE MTT-S Int. Microw. Symp. Dig.*, Jun. 2009, pp. 733–736.

[5] M. A. Morgan and T. A. Boyd, "Theoretical and experimental study of a new class of reflectionless filter," *IEEE Trans. Microw. Theory Techn.*, vol. 59, no. 5, pp. 1214–1221, May 2011.

[6] M. A. Morgan and T. A. Boyd, "Reflectionless filter structures," *IEEE Trans. Microw. Theory Techn.*, vol. 63, no. 4, pp. 1263–1271, Apr. 2015.

[7] J. Lee, B. Lee, S. Nam, and J. Lee, "Rigorous design method for symmetric reflectionless filters with arbitrary prescribed transmission response," *IEEE Trans. Microw. Theory Techn.*, vol. 68, no. 6, pp. 2300–2307, Jun. 2020.

[8] P. Ma, B. Wei, Y. Heng, C. Luo, X. Guo, and B. Cao, "Design of absorptive superconducting filter," *Electron. Lett.*, vol. 53, no. 11, pp. 728–730, May 2017.

[9] M. Fan, K. Song, L. Yang, and R. Gomez-Garcia, "Frequency-tunable constant-absolute-bandwidth single-/dual-passband filters and diplexers with all-port-reflectionless behavior," *IEEE Trans. Microw. Theory Techn.*, vol. 69, no. 2, pp. 1365–1377, Feb. 2021.

[10] D. Psychogiou and R. Gomez-Garcia, "Reflectionless adaptive RF filters: Bandpass, bandstop, and cascade designs," *IEEE Trans. Microw. Theory Techn.*, vol. 65, no. 11, pp. 4593–4605, Nov. 2017.

[11] R. Gómez-García, J. Muñoz-Ferreras, W. Feng, and D. Psychogiou, "Balanced symmetrical quasi-reflectionless single- and dual-band bandpass planar filters," *IEEE Microw. Wireless Compon. Lett.*, vol. 28, no. 9, pp. 798–800, Sep. 2018.

[12] R. Gomez-Garcia, J.-M. Munoz-Ferreras, and D. Psychogiou, "Dual-behavior resonator-based fully reconfigurable input reflectionless bandpass filters," *IEEE Microw. Wireless Compon. Lett.*, vol. 29, no. 1, pp. 35–37, Jan. 2019.

[13] R. Gómez-García, J.-M. Muñoz-Ferreras, and D. Psychogiou, "Symmetrical quasi-absorptive RF bandpass filters," *IEEE Trans. Microw. Theory Techn.*, vol. 67, no. 4, pp. 1472–1482, Apr. 2019.

[14] R. Gomez-Garcia, J.-M. Munoz-Ferreras, and D. Psychogiou, "High-order input-reflectionless bandpass/bandstop filters and multiplexers," *IEEE Trans. Microw. Theory Techn.*, vol. 67, no. 9, pp. 3683–3695, Sep. 2019.

[15] Y. Yang, M. Yu, X. Yin, and Q. Wu, "On the singly terminated and complementary networks," *IEEE Trans. Microw. Theory Techn.*, vol. 67, no. 3, pp. 988–996, Mar. 2019.

[16] X.-H. Jin, X.-D. Huang, Q. Ren, and C.-H. Cheng, "Four-port symmetrical reflectionless lumped filter/diplexer: Prototype and design table," *IEEE Trans. Microw. Theory Techn.*, vol. 69, no. 4, pp. 2211–2219, Apr. 2021.

[17] C. Liu, Z. Deng, X. Liu, and X. Luo, "A wideband bandpass filter with broad stopband and ultra-wide reflectionless range for 5G applications," in *IEEE MTT-S Int. Microw. Symp. Dig.*, Jun. 2019, pp. 834–837.

[18] W. Yu, Y. Rao, H. J. Qian, and X. Luo, "Reflectionless filtering 90° coupler using stacked cross coupled-line and loaded cross-stub," *IEEE Microw. Wireless Compon. Lett.*, vol. 30, no. 5, pp. 481–484, May 2020.

[19] C. Luo *et al.*, "Quasi-reflectionless microstrip bandpass filters using bandstop filter for out-of-band improvement," *IEEE Trans. Circuits Syst. II, Exp. Briefs*, vol. 67, no. 10, pp. 1849–1853, Oct. 2020.

[20] S.-W. Jeong, T.-H. Lee, and J. Lee, "Frequency- and bandwidth-tunable absorptive bandpass filter," *IEEE Trans. Microw. Theory Techn.*, vol. 67, no. 6, pp. 2172–2180, Jun. 2019.

[21] B. Lee, S. Nam, and J. Lee, "Filtering power divider with reflectionless response and wide isolation at output ports," *IEEE Trans. Microw. Theory Techn.*, vol. 67, no. 7, pp. 2684–2692, Jul. 2019.

[22] R. Gomez-Garcia, L. Yang, J.-M. Munoz-Ferreras, and W. Feng, "Lossy signal-interference filters and applications," *IEEE Trans. Microw. Theory Techn.*, vol. 68, no. 2, pp. 516–529, Feb. 2020.

[23] R. Gomez-Garcia, L. Yang, and J.-M. Munoz-Ferreras, "Low-reflection signal-interference single- and multipassband filters with shunted lossy stubs," *IEEE Microw. Wireless Compon. Lett.*, vol. 30, no. 4, pp. 355–358, Apr. 2020.

[24] X. Wu, Y. Li, and X. Liu, "High-order dual-port quasi-absorptive microstrip coupled-line bandpass filters," *IEEE Trans. Microw. Theory Techn.*, vol. 68, no. 4, pp. 1462–1475, Apr. 2020.

[25] X. Wu, Y. Li, and X. Liu, "Quasi-reflectionless microstrip bandpass filters with improved passband flatness and out-of-band rejection," *IEEE Access*, vol. 8, pp. 160500–160514, 2020.

[26] L. Yang, R. Gomez-Garcia, J.-M. Munoz-Ferreras, R. Zhang, D. Peroulis, and L. Zhu, "Multilayered reflectionless wideband bandpass filters with shunt/in-series resistively terminated microstrip lines," *IEEE Trans. Microw. Theory Techn.*, vol. 68, no. 3, pp. 877–893, Mar. 2020.

[27] L. Yang, R. Gomez-Garcia, J.-M. Munoz-Ferreras, and W. Feng, "Multilayered wideband balun bandpass filters designed with input-reflectionless response," in *Proc. 49th Eur. Microw. Conf. (EuMC)*, Oct. 2019, pp. 452–455.

[28] L. Yang, R. Gómez-García, J.-M. Munoz-Ferreras, and R. Zhang, "Input-reflectionless low-pass filter on multilayered diplexer-based topology," *IEEE Microw. Wireless Compon. Lett.*, vol. 30, no. 10, pp. 945–948, Oct. 2020.

[29] A. Guilabert, M. A. Morgan, and T. A. Boyd, "Reflectionless filters for generalized elliptic transmission functions," *IEEE Trans. Circuits Syst. I, Reg. Papers*, vol. 66, no. 12, pp. 4606–4618, Dec. 2019.

[30] L. Yang, R. Gomez-Garcia, and M. Fan, "Input-reflectionless balanced wideband bandpass filter using multilayered vertical transitions," in *Proc. IEEE Asia–Pacific Microw. Conf. (APMC)*, Dec. 2020, pp. 1–3.
[31] L. Zhu, S. Sun, and R. Li, *Microwave Bandpass Filters for Wideband Communications*. New York, NY, USA: Wiley, 2012.
[32] J. J. Sánchez-Martínez, E. Márquez-Segura, and S. Lucyszyn, "Synthesis and design of high-selectivity wideband quasi-elliptic bandpass filters using multiconductor transmission lines," *IEEE Trans. Microw. Theory Techn.*, vol. 63, no. 1, pp. 198–208, Jan. 2015.
[33] F. Huang, J. Wang, K. Aliqab, J. Hong, and W. Wu, "Analysis and design of a new self-packaged wideband balun bandpass filter with the functionality of impedance transformation," *IEEE Trans. Microw. Theory Techn.*, vol. 67, no. 6, pp. 2322–2330, Jun. 2019.
[34] H. Zhu, J.-Y. Lin, and Y. J. Guo, "Filtering balanced-to-single-ended power dividers with wide range and high level of common-mode suppression," *IEEE Trans. Microw. Theory Techn.*, vol. 67, no. 12, pp. 5038–5048, Dec. 2019.
[35] Y.-M. Zhang, S. Zhang, G. Yang, and G. F. Pedersen, "A wideband filtering antenna array with harmonic suppression," *IEEE Trans. Microw. Theory Techn.*, vol. 68, no. 10, pp. 4327–4339, Oct. 2020.
[36] L. Yang, L. Zhu, W.-W. Choi, and K.-W. Tam, "Analysis and design of wideband microstrip-to-microstrip equal ripple vertical transitions and their application to bandpass filters," *IEEE Trans. Microw. Theory Techn.*, vol. 65, no. 8, pp. 2866–2877, Aug. 2017.
[37] L. Yang *et al.*, "Novel multilayered ultra-broadband bandpass filters on high-impedance slotline resonators," *IEEE Trans. Microw. Theory Techn.*, vol. 67, no. 1, pp. 129–139, Jan. 2019.
[38] H. J. Carlin and W. Kohler, "Direct synthesis of band-pass transmission line structures," *IEEE Trans. Microw. Theory Techn.*, vol. MTT-13, no. 3, pp. 283–297, May 1965.
[39] R. Li, S. Sun, and L. Zhu, "Direct synthesis of transmission line low-/high-pass filters with series stubs," *IET Microw., Antennas Propag.*, vol. 3, no. 4, pp. 654–662, Jun. 2009.
[40] L. Yang, L. Zhu, W.-W. Choi, K.-W. Tam, R. Zhang, and J. Wang, "Wideband balanced-to-unbalanced bandpass filters synthetically designed with Chebyshev filtering response," *IEEE Trans. Microw. Theory Techn.*, vol. 66, no. 10, pp. 4528–4539, Oct. 2018.
[41] D. A. Frickey, "Conversions between S, Z, Y, H, ABCD, and T parameters which are valid for complex source and load impedances," *IEEE Trans. Microw. Theory Techn.*, vol. 42, no. 2, pp. 205–211, Feb. 1994.

Li Yang (Member, IEEE) received the M.Sc. degree in electrical and electronics engineering and the Ph.D. degree in electrical and computer engineering from the University of Macau (UM), Macau, China, in 2013 and 2018, respectively.

In 2018, he was a Research Associate with the Department of Electrical and Computer Engineering, UM. Since 2018, he holds a post-doctoral position with the Department of Signal Theory and Communications, University of Alcalá, Alcalá de Henares, Spain, where he is currently a GOT ENERGY TALENT (GET)-COFUND Marie Curie Fellow. His current research interests include the synthesis and design of RF/microwave planar and multilayered passive filters, reconfigurable filters, filtering antennas, and multifunctional circuits and systems.

Dr. Yang was a recipient of the Best Student Paper Award of the International Symposium on Antennas and Propagation 2010 in Macau.

Roberto Gómez-García (Senior Member, IEEE) received the Dipl.-Eng. degree in telecommunication engineering and the Ph.D. degree in electrical and electronic engineering from Polytechnic University of Madrid, Madrid, Spain, in 2001 and 2006, respectively.

Since 2006, he has been an Associate Professor with the Department of Signal Theory and Communications, University of Alcalá, Alcalá de Henares, Spain. He has been, for several research stays, with the C2S2 Department, XLIM Research Institute, University of Limoges, Limoges, France, the Telecommunications Institute, University of Aveiro, Aveiro, Portugal, the U.S. Naval Research Laboratory, Microwave Technology Branch, Washington, DC, USA, and Purdue University, West Lafayette, IN, USA. He is also an Adjunct Part-Time Professor with the University of Electronic Science and Technology of China, Chengdu, China, and has been an Invited Professor with Gdansk University of Technology, Poland, during 2019–2020. His current research interests include the design of fixed/tunable high-frequency filters and multiplexers in planar, hybrid, and monolithic microwave-integrated circuit technologies, multifunction circuits and systems, and software-defined radio and radar architectures for telecommunications, remote sensing, and biomedical applications. In these topics, he has authored/coauthored about 120 articles in international journals and 155 papers in international conferences.

Dr. Gómez-García serves as a member for the Technical Review Board for several IEEE and EuMA conferences. He is also an elected member of the IEEE MTT-S Filters (MTT-5), the IEEE MTT-S RF MEMS and Microwave Acoustics (MTT-6), the IEEE MTT-S Wireless Communications (MTT-23), the IEEE MTT-S Biological Effects and Medical Applications of RF and Microwave (MTT-28), and the IEEE CAS-S Analog Signal Processing Technical Committees. He was a recipient of the 2016 IEEE Microwave Theory and Techniques Society (MTT-S) Outstanding Young Engineer Award. He is an IEEE CAS-S Distinguished Lecturer (2020–2022). He was an Associate Editor of the IEEE TRANSACTIONS ON MICROWAVE THEORY AND TECHNIQUES from 2012 to 2016 and the IEEE TRANSACTIONS ON CIRCUITS AND SYSTEMS-I: REGULAR PAPERS from 2012 to 2015. He was a Senior Editor of the IEEE JOURNAL ON EMERGING AND SELECTED TOPICS IN CIRCUITS AND SYSTEMS from 2016 to 2017. He was a Guest Editor for several Special/Focus Issues and Sections in IEEE and IET Journals. He is currently an Associate Editor of the IEEE MICROWAVE AND WIRELESS COMPONENTS LETTERS, IEEE JOURNAL OF ELECTROMAGNETICS, RF AND MICROWAVES IN MEDICINE AND BIOLOGY, IEEE ACCESS, *IET Microwaves, Antennas, and Propagation*, TC-5 Topic Editor of IEEE JOURNAL OF MICROWAVES, and the *International Journal of Microwave and Wireless Technologies*, and the MTT-S Newsletter Working Group Chair.

Maoyu Fan was born in Chongqing, China, in 1991. She received the B.Sc. degree in physics from the University of Electronic Science and Technology of China (UESTC), Chengdu, China, in 2014, and is currently pursuing the Ph.D. degree at UESTC.

During the academic year 2019–2020, she has been a Visiting Ph.D. student at the University of Alcalá, Alcalá de Henares, Spain. Her current research interests include microwave passive and tunable filters.

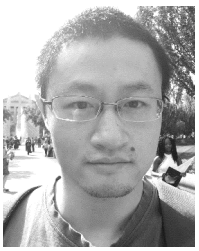

Runqi Zhang (Member, IEEE) received the B.Eng. and M.Eng. degrees in electromagnetic field and radio technology from the University of Electronic Science and Technology of China, Chengdu, China, in 2007 and 2010, respectively, and the Ph.D. degree from the School of Electrical and Electronic Engineering, Nanyang Technological University (NTU), Singapore, in 2015.

From 2014 to 2015, he was a Research Associate with the Center for Infocomm Technology, NTU. From 2015 to 2016, he was a Research Engineer and then a Research Fellow with the Satellite and Airborne Radar Systems Laboratory, National University of Singapore, Singapore. From 2016 to 2019, he was a Post-Doctoral Researcher with the Electrical and Computer Engineering, Purdue University, West Lafayette, IN, USA. Since 2019, he has been a Senior Design Engineer with Akoustis, Inc., Huntersville, NC, USA. His current research interests include satellite communication, synthesis and design of RF/microwave passive devices, LTCC applications in the RF/microwave circuit, and SAW/BAW filters.